universe

MDPI

Article

Hubble Tension as an Effect of Horizon Entanglement Nonequilibrium

Alexander S. Sakharov [1,2], Rostislav Konoplich [1,3,*], Merab Gogberashvili [4,5] and Jack Simoni [1]

[1] Department of Mathematics and Physics, Manhattan University, 4513 Manhattan College Parkway, Riverdale, NY 10471, USA; alexandre.sakharov@cern.ch (A.S.S.); jsimoni02@manhattan.edu (J.S.)
[2] Experimental Physics Department, CERN, 1211 Genève 23, Switzerland
[3] Department of Physics, New York University, 726 Broadway, New York, NY 10003, USA
[4] Faculty of Exact and Natural Sciences, Javakhishvili Tbilisi State University, Tbilisi 0179, Georgia; gogber@gmail.com
[5] Department of Elementary Particles, Andronikashvili Institute of Physics, Tbilisi 0177, Georgia
* Correspondence: rostislav.konoplich@manhattan.edu

Abstract

We propose an infrared mechanism for alleviating the Hubble constant tension, based on a small departure from entanglement equilibrium at the cosmological apparent horizon. If the horizon entanglement entropy falls slightly below the Bekenstein–Hawking value, we parametrize the shortfall by a fractional deficit $\delta(a)$ evolving with the FLRW scale factor a. The associated equipartition deficit at the Gibbons–Hawking temperature then sources a smooth, homogeneous component whose density scales as H^2/G, with a dimensionless coefficient $c_e^2(a)$ of order unity times $\delta(a)$. Because this component tracks H^2, it is negligible at early times but can activate at redshifts $z \lesssim 1$, raising the late-time expansion rate by a few percent without affecting recombination or the sound horizon. We present a minimal three-parameter activation model for $c_e^2(a)$ and derive its impact on the background expansion, the effective equation of state, and linear growth for a smooth entanglement sector. The framework predicts a small boost in $H(z)$, a mild suppression of $f\sigma_8(z)$, and a corresponding modification of the low–z distance–redshift relation. We test these predictions against current low–redshift data sets, including SN Ia distance moduli, baryon acoustic oscillation distance measurements, cosmic chronometer $H(z)$ data, and redshift space distortion constraints. We then discuss whether the H_0 tension can be consistently interpreted as a late–time, horizon–scale information deficit rather than an early universe modification.

Keywords: cosmological parameters; Hubble tension; entanglement entropy; apparent horizon thermodynamics; low-redshift cosmological probes

Check for updates

Academic Editor: Júlio César Fabris

Received: 9 May 2026
Revised: 11 June 2026
Accepted: 21 June 2026
Published: 26 June 2026

Copyright: © 2026 by the authors. Licensee MDPI, Basel, Switzerland. This article is an open access article distributed under the terms and conditions of the Creative Commons Attribution (CC BY) license.

1. Introduction

A persistent discrepancy has emerged between the Hubble constant inferred from early universe probes and the value obtained from late-time distance ladders, a percent level tension that, if not due to unrecognized systematics, hints at new physics in the cosmic expansion history. Concretely, the CMB anisotropy spectrum tightly constrains the angular acoustic scale and, within a specified background model, translates this into an inferred H_0 through the sound horizon and the late–time distance to last scattering. For example, *Planck* 2018 (under ΛCDM) finds $H_0 = 67.4 \pm 0.5\,\mathrm{km\,s^{-1}\,Mpc^{-1}}$ [1], whereas local distance ladder calibrations anchored by geometric and stellar standardization methods yield higher values;

in particular, SH0ES reports $H_0 = 73.30 \pm 1.04\ \mathrm{km\,s^{-1}\,Mpc^{-1}}$ [2]. At intermediate redshifts, baryon acoustic oscillations (BAOs) provide a robust standard ruler that strongly constrains the late-time distance-redshift relation; recent DESI BAO constraints favor values closer to the *Planck* inferred scale [3,4], sharpening the question of whether a consistent cosmological history can reconcile early- and late-time determinations. Explanations proposed so far broadly fall into two classes. Early-time modifications (e.g., early dark energy, extra radiation, or altered recombination) reduce the sound horizon so the CMB can accommodate a larger H_0, while late-time ideas (e.g., evolving dark energy or modified gravity) adjust the low-z Hubble rate with minimal impact on recombination; see Refs. [5–11] for reviews. Both directions face tight joint constraints from CMB anisotropies, BAO, Type-Ia supernova distances, and structure growth observables: DESI BAO remain consistent with flat ΛCDM and bound w near -1, Pantheon+ tightens the low-z distance–redshift relation, and redshift distortion (RSD) growth measurements strongly restrict early-time solutions such as EDE when combined with CMB data [3,4,9,12–16].

In parallel, advances in quantum information and gravity have reshaped how we think about spacetime: horizons carry entropy and temperature; entanglement can encode geometry; and thermodynamic reasoning can reproduce gravitational dynamics. However, naive free-field entanglement in curved spacetime contributes only $\mathcal{O}(H^4)$ to the vacuum energy, which is far too small to matter cosmologically, and the ultra violet (UV) area law renormalizes $1/G$ rather than producing a new fluid. Any entanglement-driven mechanism relevant to the Hubble tension must therefore be infrared (IR) and horizon tied, not a re-counting of UV modes.

We develop and assess such an IR mechanism: the horizon entanglement equipartition deficit (HEED). The core hypothesis is that the quantum state of our late-time universe is slightly out of entanglement equilibrium at the apparent (Hubble) horizon. If the actual horizon entanglement entropy S_{ent} falls short of the Bekenstein–Hawking value $S_{\mathrm{BH}} = A/(4G)$ by a fractional deficit $\delta(a) \in [0, 1]$, then when treating the horizon as an entanglement screen at the Gibbons–Hawking temperature $T_{\mathrm{dS}} = H/(2\pi)$, the resulting equipartition deficit translates into a homogeneous bulk component of density

$$\rho_{\mathrm{HEED}}(a) = \frac{3}{8\pi G}\, c_e^2(a)\, H^2(a), \qquad c_e^2(a) \sim \mathcal{O}(1) \times \delta(a), \tag{1}$$

where $H(a)$ stand for the Hubble rate evolving with the FLRW scale factor a. This is the familiar holographic H^2/G [17–20], but with a time-dependent coefficient tied to horizon entanglement rather than an ad hoc constant.

Two features make HEED cosmologically attractive. First, because $\rho_{\mathrm{HEED}} \propto H^2$, it is automatically negligible at high redshift relative to matter and radiation, thereby preserving recombination physics and the sound horizon. Second, we model a late–time activation of the HEED amplitude by letting

$$c_e^2(a) = c_{e0}^2\, g(a; a_t, k), \tag{2}$$

where the dimensionless switch function $g(a; a_t, k)$ interpolates smoothly from $g \ll 1$ at early times ($a \ll a_t$) to $g \to 1$ at late times ($a \gtrsim a_t$). The parameter a_t sets the characteristic activation epoch (equivalently $z_t \simeq a_t^{-1} - 1$), while k controls the sharpness of the transition (larger k corresponds to a steeper switch). This late activation can yield a few percent increase in the low–z Hubble rate, sufficient to ease the tension while remaining consistent with SN/BAO distances. Interpreted as a smooth, non–clustering sector (rest–frame sound speed $\simeq 1$), HEED modestly suppresses structure growth through $f\sigma_8$, providing additional levers beyond purely geometric constraints.

Conceptually, HEED can be read in two equivalent ways. In a fluid picture, $\rho_{\rm HEED}$ adds to the stress–energy budget and the Friedmann equation becomes

$$H^2(a) = \frac{8\pi G}{3}\,\frac{\rho_m(a)+\rho_\Lambda}{1-c_e^2(a)}\,, \tag{3}$$

where $\rho_m(a) = \rho_{m0}\,a^{-3}$ is the (pressureless) matter density, and $\rho_\Lambda \equiv \Lambda/(8\pi G)$ is the vacuum energy density associated with the cosmological constant. The entanglement deficit therefore appears as a multiplicative correction to the expansion rate. In a modified gravity reading, the same factor reshapes the effective Planck mass, $M_*^2(a) = M_{\rm Pl}^2\,[1-c_e^2(a)]$, while matter remains covariantly conserved. Either view preserves the Bianchi identity and avoids ghost/gradient instabilities so long as the entanglement sector is treated as smooth and non–propagating (an effective IR dressing of the background rather than a new field).

This paper makes the following contributions. We formalize HEED from horizon thermodynamics and entanglement equilibrium, clarifying the UV/IR split: UV area law pieces renormalize $1/G$, whereas the IR deficit $\delta(a)$ sources $\rho \propto H^2/G$. We derive background relations' closed form, an instantaneous effective $w_{\rm HEED}(a)$, and the logarithmic derivative $d\ln H/d\ln a$ needed for growth under a minimal three parameter activation $\{c_{e0}^2, a_t, k\}$. We analyze linear perturbations with a smooth entanglement sector, predicting a characteristic pattern: small late-time boosts to $H(z)$ and mild suppression of $f\sigma_8$. We confront the model with low–redshift data by fitting SN Ia, BAO, and cosmic chronometer (CC) constraints together with a CMB distance prior that keeps the sound horizon fixed, and by testing the resulting growth history against RSD measurements, while imposing the early-time safety condition $c_e^2(a_\star) \ll 1$ at recombination.

HEED sits at the intersection of holographic dark energy (HDE)-type scalings and entanglement equilibrium thinking. Unlike standard HDE with a constant c^2, HEED explains the coefficient as a dynamical horizon information shortfall that can switch on at $z \lesssim 1$. Unlike free field "entanglement dark energy," it avoids the $\mathcal{O}(H^4)$ suppression by tying directly to the horizon's IR thermodynamics.

It is important to note that the present work should be viewed as an effective IR cosmological parametrization motivated by horizon thermodynamics and entanglement equilibrium, rather than as a complete microscopic holographic dual or a UV-complete local field theory. Its purpose is to isolate the phenomenological consequences of a small late-time horizon entanglement deficit, clarify the associated UV/IR split, and test whether such a component can remain consistent with current low-redshift distance and growth data. This effective IR status is not unusual in cosmology: many dark-energy and modified-gravity models were analyzed extensively at the phenomenological level before any full UV completion or microscopic derivation was available, including early dark energy, interacting dark energy, phenomenological growth frameworks, $f(R)$ gravity, emergent dark energy, modified-gravity interpretations of late-time data, effective running Hubble constant, and slow-rolling scalar dynamics [21–38].

Recent alternatives to standard EDE include positive pressure barotropic components [39], transition-based dynamical dark energy with AdS-to-dS or dS-to-dS evolution [40], and HDE models with different infrared cutoffs [41]. HEED is also infrared-motivated, but it is tied to the apparent horizon and interprets the late-time correction as a finite entanglement equipartition deficit.

This paper is organized as follows. Section 2 derives HEED from horizon thermodynamics and entanglement considerations, establishes the characteristic H^2/G scaling, and clarifies the required UV/IR separation; it also presents the background dynamics, the instantaneous effective equation of state, and the minimal activation parameterization. Section 3 confronts the HEED activation parameters with a combination of four low-z

probes. The Bayesian inference framework is described in Section 3.1, where the posterior is sampled with the affine-invariant ensemble sampler `emcee`. Marginalized constraints and triangle plots are obtained with `GetDist` and interpreted in Section 3.2, which discusses posterior constraints and the internal consistency of the HEED picture. Section 4 summarizes the main results and outlines directions for future work.

2. Horizon Entanglement Equipartition Deficit

The HEED framework starts from the observation that, in a spatially flat FLRW universe, the apparent (Hubble) horizon behaves thermodynamically: it has a well-defined area and an associated temperature and entropy, in direct analogy with de Sitter and black hole horizons [42–45]. We posit that the renormalized bulk entanglement entropy of quantum fields across this horizon is slightly below the Bekenstein–Hawking value [42–45]. This small shortfall, which we call an "entanglement deficit", encodes a departure from entanglement equilibrium and, when translated through horizon equipartition [46–49], manifests as an infrared, horizon-tied contribution to the cosmic energy budget whose magnitude tracks the square of the expansion rate as H^2/G. Because this contribution is naturally tiny at early times and only becomes relevant as the universe accelerates, it can modify the late-time expansion without upsetting recombination physics, unlike free field vacuum effects whose influence scales much more weakly with the Hubble rate (see Appendix A for details).

Let Σ_H denote the apparent (Hubble) horizon on a constant time FLRW slice, and decompose the Cauchy slice into an inside region $\mathcal{R}_{\rm in}$ bounded by Σ_H and its complement $\mathcal{R}_{\rm out}$. In a QFT without gauge constraints, one may (formally) factorize the Hilbert space as $\mathcal{H} \simeq \mathcal{H}_{\rm in} \otimes \mathcal{H}_{\rm out}$; with gauge or gravitational constraints, it is cleaner to work with local operator algebras (possibly with a shared center or edge modes on Σ_H) that reproduce the usual reduced-state construction [50–52]. The global (total) state $\rho_{\rm tot}$ is a positive, unit-trace operator on the full Hilbert space, $\mathrm{Tr}\,\rho_{\rm tot} = 1$. Tracing out exterior degrees of freedom defines the reduced inside state

$$\rho_{\rm in}(a) \;\equiv\; \mathrm{Tr}_{\rm out}\,\rho_{\rm tot}(a), \tag{4}$$

and the entanglement entropy across Σ_H is

$$S_{\rm ent}(a) \;=\; -\mathrm{Tr}_{\rm in}\,\rho_{\rm in}(a)\,\ln\rho_{\rm in}(a). \tag{5}$$

As in flat space, vacuum entanglement entropy across a smooth surface exhibits an area-law divergence [50,53,54],

$$S_{\rm ent}^{\rm bare} \;=\; \eta\,\frac{A(\Sigma_H)}{\epsilon^2} + \cdots, \tag{6}$$

with nonuniversal coefficient η and cutoff ϵ. In semiclassical gravity, the same UV modes that produce the area term renormalize the Einstein–Hilbert coupling, so the generalized entropy relevant for horizon thermodynamics reads

$$S_{\rm gen}[\Sigma_H] \;=\; \frac{A(\Sigma_H)}{4\,G_{\rm ren}} + S_{\rm bulk}^{\rm ren}[\Sigma_H] + \cdots, \tag{7}$$

where the divergence has been absorbed into $G_{\rm ren}$, and $S_{\rm bulk}^{\rm ren}$ is the finite, IR-renormalized bulk entropy term associated with quantum fields across Σ_H [55–58]. In what follows, $S_{\rm ent}(a)$ denotes this renormalized IR contribution,

$$S_{\rm ent}(a) \;\equiv\; S_{\rm bulk}^{\rm ren}[\Sigma_H(a)], \tag{8}$$

which we compare to the Bekenstein–Hawking value $S_{\rm BH} = A(\Sigma_H)/(4\,G_{\rm ren})$. Departures from entanglement equilibrium are then captured by the fractional deficit

$$\delta(a) \;\equiv\; 1 - \frac{S_{\rm ent}(a)}{S_{\rm BH}(a)} \in [0,1], \tag{9}$$

with $\delta = 0$ expected in exact de Sitter and $\delta > 0$ natural out of equilibrium at late times [59,60]. In this sense, the entanglement deficit is not introduced as an additional UV area-law contribution, which is already absorbed into $G_{\rm ren}$, but as a finite infrared departure from horizon entanglement saturation. The proposal is therefore intrinsically an effective late-time parametrization of nonequilibrium horizon thermodynamics. Using the apparent horizon temperature $T_{\rm dS} = H/(2\pi)$ [42], we will map this deficit to a smooth IR component scaling as H^2/G.

To construct the HEED term, we treat the apparent horizon as an entanglement screen with area and temperature

$$A = \frac{4\pi}{H^2}, \qquad T_{\rm dS} = \frac{H}{2\pi}, \tag{10}$$

and Bekenstein–Hawking entropy $S_{\rm BH} = A/(4G)$ [42–45]. Calling it an entanglement screen means we regard the horizon as the codimension one surface across which we compute the (renormalized) bulk entanglement $S_{\rm ent}$ of quantum fields. The screen then supplies a "bookkeeping device" for associating a surface energy via equipartition to the bulk IR component. This language is in line with horizon thermodynamics, holographic ideas, and (membrane paradigm) coarse graining of horizon effective surface degrees of freedom dofs [46–49,61–64].

Following the emergent gravity/equipartition literature, we count the dofs as[1]

$$N_{\rm surf} \;=\; \frac{A}{L_p^2} \;=\; \frac{A}{G} \;=\; \frac{4\pi}{G\,H^2} \;=\; 4\,S_{\rm BH}, \tag{11}$$

which follows directly from the area law for $S_{\rm BH}$ [43,45]. This is a coarse grained count that does not assume a specific microscopic model and is routinely employed in horizon equipartition derivations of gravitational dynamics [46–49]. We then assume equipartition on the screen,

$$E_{\rm surf} \;=\; \tfrac{1}{2}\,N_{\rm surf}\,T_{\rm dS}, \tag{12}$$

with de Sitter temperature $T_{\rm dS} = H/(2\pi)$ [42]. If only a fraction $1-\delta(a)$ of these dofs are entanglement active, the missing (deficit) energy on the screen is

$$\Delta E_{\rm surf} = \tfrac{1}{2}\,\delta(a)\,N_{\rm surf}\,T_{\rm dS} = \delta(a)\,\frac{1}{G\,H}, \tag{13}$$

where the last equality follows from inserting $N_{\rm surf}$ in Equation (11) and $T_{\rm dS} = H/(2\pi)$. Associating this with a homogeneous bulk component within the Hubble volume $V_H = \frac{4\pi}{3}H^{-3}$ gives

$$\rho_{\rm HEED}(a) = \frac{\Delta E_{\rm surf}}{V_H} = \frac{3}{4\pi}\,\delta(a)\,\frac{H^2(a)}{G} = \frac{3}{8\pi G}\,c_e^2(a)\,H^2(a), \qquad c_e^2(a) \equiv 2\,\delta(a), \tag{14}$$

up to an overall numerical convention of order unity. This realizes the familiar holographic H^2/G scaling while anchoring it to IR horizon entanglement rather than to the UV area law, whose divergence renormalizes $1/G$ and therefore does not represent a dynamical fluid [55–57]. Our statement that HEED "anchors" this scaling to IR entanglement means the following: instead of postulating $\rho \propto H^2$, we derive it from the horizon's thermodynamics and a finite, IR-entanglement deficit $S_{\rm ent} < S_{\rm BH}$, via the equipartition argument

in the text. By contrast, the UV area law term in $S_{\rm ent}$ is regulator dependent and simply renormalizes $1/G$; it is not a dynamical fluid [55–57]. Thus, HEED ties the coefficient to a physical deficit $\delta(a)$, rather than treating c_e^2 as an external constant.

There are two equivalent but conceptually distinct embeddings of Equation (14) in FLRW. In a fluid (additive) view one writes

$$H^2(a) = \frac{8\pi G}{3}\big[\rho_m(a) + \rho_\Lambda + \rho_{\rm HEED}(a)\big], \qquad \rho_{\rm HEED}(a) = \frac{3}{8\pi G}\, c_e^2(a) H^2(a), \tag{15}$$

which leads to the relation

$$H^2(a) = \frac{8\pi G}{3}\, \frac{\rho_m(a) + \rho_\Lambda}{1 - c_e^2(a)}. \tag{16}$$

Alternatively, in a modified-gravity (multiplicative) view, one moves the factor $1 - c_e^2(a)$ to the geometric side and interprets it as a slowly varying Planck mass [65,66], $M_*^2(a) = M_{\rm Pl}^2[\,1 - c_e^2(a)\,]$. In either interpretation the Bianchi identity is respected and matter remains covariantly conserved, $\dot\rho_m + 3H\rho_m = 0$[2]. Early-time safety is guaranteed by requiring $c_e^2(a_\star) \ll 1$ at recombination so the sound horizon and CMB acoustic physics remain unchanged.

For phenomenology we model a smooth late-time activation as follows,

$$c_e^2(a) = c_{e0}^2\, g(a), \qquad g(a) = \frac{1 + (a_t)^k}{1 + (a_t/a)^k}, \qquad g(1) = 1, \tag{17}$$

with $a_t \in [0.4, 0.8]$, and $k \gtrsim 3$. The normalization $g(1) = 1$ makes $c_{e0}^2 = c_e^2(a = 1)$ the present day HEED fraction. Equation (16) rescales the Friedman equation by the factor

$$Q^2(a) \equiv \frac{H^2(a)}{H_0^2} = \frac{\Omega_m a^{-3} + \Omega_\Lambda}{1 - c_{e0}^2\, g(a)}, \qquad \Omega_\Lambda = 1 - \Omega_m\,. \tag{18}$$

An instantaneous effective equation of state for the HEED sector follows from $\rho_{\rm HEED} \propto H^2 c_e^2$,

$$w_{\rm HEED}(a) = -1 - \frac{1}{3}\frac{d}{d\ln a}\ln\big[Q^2(a) c_e^2(a)\big] = -1 - \frac{1}{3}\left(\frac{d\ln Q^2}{d\ln a} + \frac{d\ln c_e^2}{d\ln a}\right), \tag{19}$$

with

$$\frac{d\ln Q^2}{d\ln a} = \frac{-3\,\Omega_m a^{-3}}{\Omega_m a^{-3} + \Omega_\Lambda} + \frac{1}{1 - c_e^2(a)}\,\frac{dc_e^2(a)}{d\ln a}. \tag{20}$$

Once c_e^2 has saturated ($d\ln c_e^2/d\ln a \simeq 0$), one finds $w_{\rm HEED} \approx -1 - \frac{1}{3}\, d\ln Q^2/d\ln a \approx -1 + \Omega_m(a)$, i.e., quintessence-like behavior today for $\Omega_{m0} \simeq 0.3$. It is important to stress that this equation of state is not introduced as an independent microphysical assumption. Once $\rho_{\rm HEED}$ is fixed by the horizon equipartition ansatz, the effective pressure is determined by the continuity equation. The HEED sector is therefore covariantly conserved at the homogeneous level by construction. A derivation of $c_e^2(a)$ from a microscopic covariant action or entropy functional remains an open theoretical problem.

During the switch on ($d\ln c_e^2/d\ln a > 0$), a transient $w_{\rm HEED} < -1$ can occur. This phantom behavior pertains only to the background effective equation of state, and, because HEED introduces no propagating field, it does not signal a ghost. A ghost is a propagating mode with a negative kinetic term, which renders the Hamiltonian unbounded. In a canonical single field, achieving $w < -1$ indeed requires the wrong sign kinetic term and is pathological [69], and k-essence generically cannot stably cross $w = -1$ without ghost/gradient problems [70]. By contrast, within the EFT/Horndeski framework one can realize an effective $w_{\rm eff} < -1$ while remaining ghost free provided the kinetic matrices are positive, the scalar sound speed satisfies $c_s^2 > 0$, and the effective Planck mass remains

positive ($M_*^2 > 0$), e.g., in the α-parameterization [65,66,71–74]. HEED belongs to this safe class: it is an effective, nonpropagating IR sector equivalent to a mild time variation of $M_*^2(a) = M_{\rm Pl}^2[1 - c_e^2(a)]$ with $0 \le c_e^2(a) < 1$, so any transient $w_{\rm HEED} < -1$ during the switch-on of $c_e^2(a)$ is a kinematic background effect rather than a ghost instability. Taking $\alpha_T = 0$ and $\alpha_B \simeq \alpha_K \simeq 0$[3] keeps the extra scalar nondynamical while satisfying standard no-ghost/no-gradient conditions [65,66].

In the HEED framework we treat the entanglement sector as smooth (non-clustering) and work in GR for linear perturbations. The matter growth factor $D(a)$ (normalized so that $D(1) = 1$) obeys the standard ODE

$$D'' + \left[2 + \frac{d\ln H}{d\ln a}\right] D' - \frac{3}{2}\,\Omega_m(a)\, D = 0, \qquad \Omega_m(a) = \frac{\Omega_m a^{-3}}{Q^2(a)}, \tag{21}$$

with primes denoting $d/d\ln a$ and initial conditions set deep in matter domination[4]. Defining the dimensionless logarithmic growth rate

$$f(a) \;\equiv\; \frac{d\ln D}{d\ln a}, \tag{22}$$

and the fluctuation amplitude within $8\,h^{-1}$Mpc spheres (with $h \equiv H_0/100\,{\rm km\,s^{-1}\,Mpc^{-1}}$ the reduced Hubble constant),

$$\sigma_8(a) \;\equiv\; \sigma_{8,0}\, D(a), \tag{23}$$

the RSD observable is the product $f\sigma_8(z)$ which is robust to linear galaxy bias and is widely used to test late-time dynamics [77,78]. For HEED backgrounds,

$$\frac{d\ln H}{d\ln a} = \frac{1}{2}\frac{d\ln Q^2}{d\ln a} = -\frac{3}{2}\,\Omega_m(a) \;+\; \frac{1}{2}\,\frac{dc_e^2/d\ln a}{1 - c_e^2}\,, \tag{24}$$

so the "friction" term in Equation (21) is slightly enhanced during the HEED switch on ($dc_e^2/d\ln a > 0$), yielding a mild suppression of growth relative to ΛCDM at $z \lesssim 1$. Once $c_e^2(a)$ saturates ($dc_e^2/d\ln a \simeq 0$), the growth history closely tracks that of a smooth dark energy model with the same $Q(a)$. A useful approximation for intuition is the growth index form $f(a) \simeq \Omega_m(a)^\gamma$ with $\gamma \simeq 0.55$ in GR and small, $w(a)$-dependent corrections for smooth dark energy [77]. The HEED behaves like such a smooth sector and therefore predicts percent-level shifts in $f\sigma_8(z)$ concentrated at low redshift (as illustrated in Figure 1).

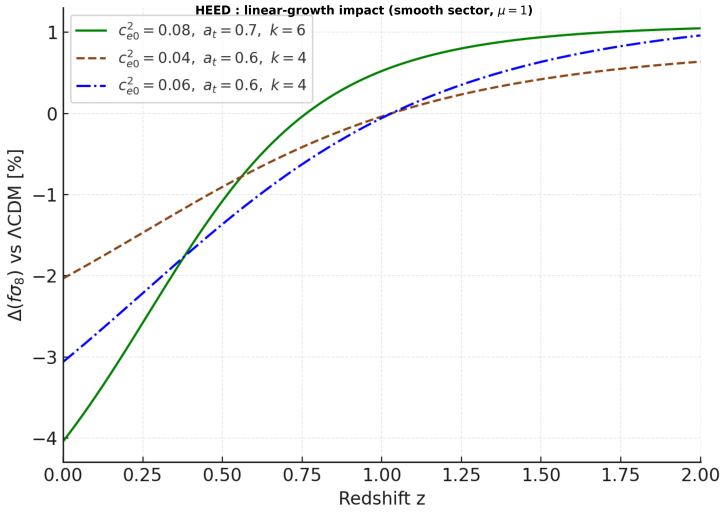


Figure 1. HEED's linear growth impact illustrated for three sets of the activation parameters.

These features have clear observational implications. At $a = 1$, Equation (18) gives $Q^2(1) = 1/(1 - c_{e0}^2)$, so the inferred Hubble constant is boosted by $H_0^{(\mathrm{eff})}/H_0 = (1 - c_{e0}^2)^{-1/2}$, as illustrated in Figure 2. A modest $c_{e0}^2 = 0.06$ yields a $\sim 3.1\%$ increase, while $c_{e0}^2 = 0.10$ gives $\sim 5.3\%$. Because $g(a \ll a_t) \ll 1$, recombination era distances and the sound horizon remain essentially unchanged, providing exactly the lever arm required by the early–late H_0 discrepancy. Low-redshift distance indicators (SN/BAO) can be matched with gentle adjustments driven by the amplitude of c_{e0}^2 and parameters a_t and k describing the activation history. A practical data strategy is to fit SN + BAO + CC backgrounds with a CMB distance prior to keep the sound horizon r_d standard; then, test RSD $f\sigma_8(z)$ [78,79], enforcing the early-time prior $c_e^2(a_\star) \ll 1$ at recombination.

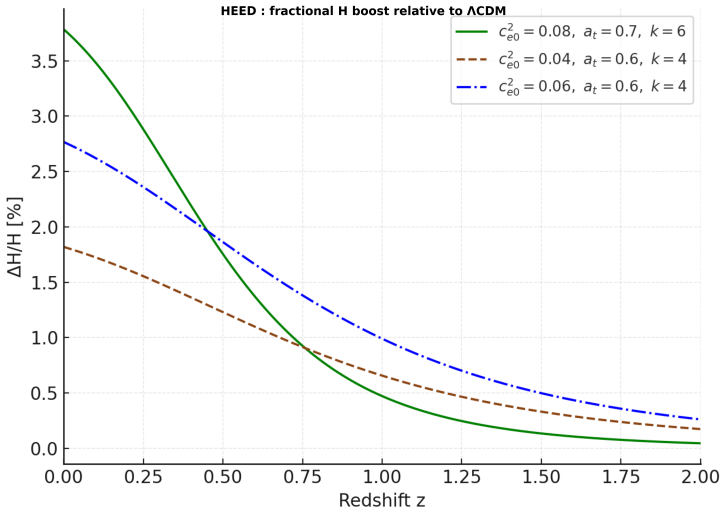


Figure 2. HEED-corrected low-redshift Hubble constant related via its residuals relative to the ΛCDM calculations.

The construction developed above is restricted to homogeneous, spatially flat FLRW cosmology and the apparent (Hubble) horizon. No fully covariant extension to generic spacetimes is assumed here; the present aim is instead to formulate and test the corresponding effective infrared cosmological dynamics in the simplest setting relevant to the Hubble tension.

Finally, we note relationships and distinctions with neighboring ideas. Modular Hamiltonian first-law analyses for ball regions show that free or conformal fields produce $\delta\rho \sim H^4$ corrections [80–85] (see Appendix A for details), which are far too small to be cosmologically relevant; HEED avoids this suppression by tying the effect to IR horizon thermodynamics. Standard holographic dark energy simply posits $\rho \propto H^2/G$ with a constant coefficient; HEED explains the coefficient as a time-dependent horizon entanglement shortfall $c_e^2(a) = 2\,\delta(a)$ with a natural late-time activation. The framework is local in time (apparent horizon) and thus avoids teleological issues associated with future event horizons [42,46,49,86]. In sum, HEED constitutes a thermodynamically motivated, IR-entanglement mechanism that is internally consistent (conservation, stability, and horizon thermodynamics), naturally small at high redshift, and predictive for late-time expansion and linear growth [86].

3. Observational Consistency Analysis

In this section we confront the HEED activation parameter triplet with a combination of four low-z probes, treated as independent Gaussian constraints. We use SN Ia distance moduli $\mu(z)$ from Pantheon+ [12,87]; cosmic–chronometer (CC) determinations of $H(z)$ from differential age measurements of passively evolving early-type galaxies [88–94];

compressed BAO measurements of the transverse comoving distance $d_M(z)/r_d$ and the radial comoving Hubble distance $d_H(z)/r_d$ from BOSS DR12 [13], eBOSS DR16 [14] and DESI DR2 [4], adopting a fixed sound horizon r_d [1]; and RSD measurements of the growth rate $f\sigma_8(z)$ from BOSS/eBOSS [13,95–100], together with WiggleZ [101], VIPERS [102–107], supplemented by very low-z [108–112] and high-z [113–116] constraints.

For the CC sample we employ the community "classic" 31-point set, typically treated as uncorrelated and assembled from DA measurements (see Table A1 in Appendix B); in this approach the redshift–age relation yields dz/dt, which is converted to the Hubble parameter via $H(z) = -(1+z)^{-1}\, dz/dt$. The BAO observables used here are compiled from Refs. [4,13,14], with the full list of points provided in Table A2 of Appendix B. Finally, Table A3 of Appendix B presents a consolidated set of 63 RSD measurements of the linear growth rate, reported as $f\sigma_8(z)$ with 1σ uncertainties and spanning $z \simeq 0.001$–1.944, compiled in Ref. [117]. This compilation includes very low-z peculiar velocity and Tully–Fisher constraints from 2MTF [108], 2MRS [109,110], and 6dFGS/6dFGS+SNe [111,112]; early RSD determinations from SDSS–LRG [118] (including the SDSS–LRG–200/60 re-analyses [119]) and DR7–LRG [120]; low-z galaxy-survey results from SDSS–MGS [121], SDSS–veloc [122], DR13 [123], and GAMA [124]; the WiggleZ three-point set [101]; extensive BOSS measurements, namely LOWZ/CMASS and DR10–DR12 from Refs. [13,14,95–100]; multiple VIPERS determinations (including v7 and PDR–2) [102–107]; additional SDSS DR7 peculiar-velocity work [125]; the FastSound high-z constraint [113]; and the SDSS–IV QSO tomographic measurements at $z = 0.978$, 1.23, 1.526, 1.944 [114–116].

Distances follow the standard flat FLRW relations with $H(z)$ defined in Equations (17) and (18):

$$d_C(z) = \int_0^z \frac{c\, dz'}{H(z')}, \qquad d_M(z) = d_C(z), \qquad d_L(z) = (1+z) d_M(z), \qquad \mu(z) = 5\log_{10}\big(D_L/\mathrm{Mpc}\big) + 25. \tag{25}$$

BAO observables are d_M/r_d and d_H/r_d with $d_H \equiv c/H$.

We analyze HEED in the additive embedding at the level of the homogeneous background, in which the entanglement sector contributes an algebraic H^2-proportional term to the Friedmann equation expressed by Equation (15). Eliminating ρ_{HEED} gives the closed background relation expressed by Equation (18). We normalize the activation so that $c_e^2(a=1) = c_{e0}^2$, and parameterize

$$c_e^2(a) = c_{e0}^2\, g(a), \tag{26}$$

with $g(1) = 1$ and a late-time switch-on controlled by (a_t, k), as in Equation (17). In this embedding it is convenient to define the effective late-time Hubble scale,

$$H_0^{\mathrm{eff}} \equiv H(a=1) = \frac{H_0}{\sqrt{1 - c_{e0}^2}}, \tag{27}$$

which is the quantity constrained by local measurements. Linear growth assumes a smooth, non-clustering HEED sector in general relativity (GR) so that the growth factor $D(a)$ satisfies Equation (21) integrated from matter domination with $D(a=1) = 1$. The RSD prediction is

$$f\sigma_8(z) = \left.\frac{d\ln D}{d\ln a}\right|_{a=1/(1+z)} \sigma_{8,0}\, D\!\left(a = \frac{1}{1+z}\right), \tag{28}$$

with $\sigma_{8,0}$ held fixed as a Gaussian prior.

3.1. Bayesian Formulation

The baseline parameter vector in use is

$$\boldsymbol{\theta} = \{H_0, \Omega_m, c_{e0}^2, a_t, k, \sigma_8\}, \tag{29}$$

where H_0 is the underlying Hubble constant entering Equation (18), while $H_0^{\rm eff}$ is given by Equation (27). The data vector $\mathbf{d} = \{\boldsymbol{\mu}^{\rm obs}, \mathbf{b}^{\rm obs}, \mathbf{h}^{\rm obs}, \mathbf{g}^{\rm obs}\}$ collects SN Ia distance moduli $\boldsymbol{\mu}^{\rm obs}$, BAO points $\mathbf{b}^{\rm obs} \equiv \{D_M/r_d,\, D_H/r_d\}$, CC measurements $\mathbf{h}^{\rm obs} \equiv \{H(z)\}$, and RSD growth measurements $\mathbf{g}^{\rm obs} \equiv \{f\sigma_8(z)\}$. For a given $\boldsymbol{\theta}$, the corresponding predictions $\boldsymbol{\mu}^{\rm th}(\boldsymbol{\theta})$, $\mathbf{b}^{\rm th}(\boldsymbol{\theta})$, $\mathbf{h}^{\rm th}(\boldsymbol{\theta})$, and $\mathbf{g}^{\rm th}(\boldsymbol{\theta})$ are computed from $H(z;\boldsymbol{\theta})$ via Equations (21), (25) and (28).

We define the posterior as

$$\mathcal{P}(\boldsymbol{\theta} \mid \mathbf{d}) \;\propto\; \mathcal{L}(\mathbf{d} \mid \boldsymbol{\theta})\, \Pi(\boldsymbol{\theta}), \qquad \ln \mathcal{L} = -\tfrac{1}{2}\, \chi^2_{\rm tot}(\boldsymbol{\theta}), \tag{30}$$

with the total quadratic statistic

$$\chi^2_{\rm tot}(\boldsymbol{\theta}) = \chi^2_{\rm SN} + \chi^2_{\rm BAO} + \chi^2_{\rm CC} + \chi^2_{\rm RSD} + \chi^2_{\sigma_8} + \chi^2_{\rm prior}, \tag{31}$$

assuming Gaussian errors and (for this baseline analysis) independence between data blocks.

The SN term uses Hubble diagram residuals and profiles out a single additive offset ΔM, encoding the absolute magnitude (distance zero-point) degeneracy with the Hubble scale. With diagonal errors the raw statistic is

$$\chi^2_{\rm SN}(\boldsymbol{\theta}, \Delta M) = \sum_i \frac{\left[\mu_i - \mu_{\rm th}(z_i;\boldsymbol{\theta}) - \Delta M\right]^2}{\sigma^2_{\mu,i}}, \tag{32}$$

where $\mu_{\rm th}(z)$ is evaluated from $H(z)$. Minimization of Equation (32) with respect to ΔM yields the analytic profiler

$$\Delta M^\star(\boldsymbol{\theta}) = \frac{\sum_i \left[\mu_i - \mu_{\rm th}(z_i;\boldsymbol{\theta})\right]/\sigma^2_{\mu,i}}{\sum_i 1/\sigma^2_{\mu,i}}, \qquad \chi^2_{\rm SN}(\boldsymbol{\theta}) \equiv \chi^2_{\rm SN}\big(\boldsymbol{\theta}, \Delta M^\star(\boldsymbol{\theta})\big), \tag{33}$$

which is equivalent to analytically marginalizing over a constant offset with a flat prior. Operationally, we profile separately for each cosmological model (HEED and ΛCDM), so each curve is shifted by its own $\Delta M^\star$, consistent with standard practice in compressed SN likelihood applications [12,87]. Consequently, SN data alone do not fix H_0; the absolute scale is set only when combined with an absolute ruler such as CC or BAO (through r_d), or by including an explicit external anchor.

The BAO and CC blocks adopt diagonal Gaussian forms,

$$\chi^2_{\rm BAO} = \sum_j \left[\frac{\left(d_M(z_j)/r_d - (d_M/r_d)_{\rm obs}\right)^2}{\sigma^2_{d_M/r_d,j}} + \frac{\left(d_H(z_j)/r_d - (d_H/r_d)_{\rm obs}\right)^2}{\sigma^2_{d_H/r_d,j}} \right], \tag{34}$$

$$\chi^2_{\rm CC} = \sum_\ell \frac{\left(H(z_\ell) - H_{\rm obs}\right)^2}{\sigma^2_{H,\ell}}, \tag{35}$$

which are the diagonal-covariance limits of the standard Gaussian likelihood

$$\chi^2 = \Delta\mathbf{d}^{\,T}\mathbf{C}^{-1}\Delta\mathbf{d}, \qquad \Delta\mathbf{d} \equiv \mathbf{d}^{\rm obs} - \mathbf{d}^{\rm th}(\boldsymbol{\theta}), \tag{36}$$

where $\mathbf{C}$ is the covariance matrix of the corresponding data vector. Equations (34) and (35) therefore amount to taking $\mathbf{C}$ to be diagonal, with entries given by the reported variances.

The corresponding growth log-likelihood is taken as

$$\chi^2_{\rm RSD} = \sum_m \frac{\left[f\sigma_8(z_m;\boldsymbol{\theta}) - (f\sigma_8)_{\rm obs}\right]^2}{\sigma^2_{f\sigma_8,m}}, \tag{37}$$

with diagonal errors in this baseline implementation. In practice, the RSD block provides the primary handle on late-time structure growth in our low-z data combination, since the predicted $f\sigma_8(z)$ is obtained by solving the linear growth equation with coefficients determined by the background expansion $H(z)$. Within the assumptions of GR growth and a smooth (non-clustering) HEED sector, this term therefore links the background parameters controlling $H(z)$ to the growth history encoded in $D(a)$ and $f \equiv d\ln D/d\ln a$.

To regularize the growth sector, we include a weak Gaussian prior on σ_8,

$$\chi^2_{\sigma_8} = \left(\frac{\sigma_8 - \sigma_{8,\star}}{\sigma_{\sigma_8}}\right)^2, \tag{38}$$

which may be chosen to be broad enough to avoid importing CMB-dominated information, yet prevents unphysical excursions when the RSD block alone is insufficient to pin down σ_8 in combination with $(\Omega_m, c^2_{e0}, a_t, k)$.

We include three priors/guards, assembled as

$$\chi^2_{\rm prior} = \chi^2_{\rm early} + \chi^2_{\rm wall} + \chi^2_{H_0^{\rm eff}}. \tag{39}$$

The early-time prior enforces negligible HEED at recombination,

$$\chi^2_{\rm early} = \begin{cases} 0, & c^2_e(a_\star) \le \varepsilon, \\ \left(\dfrac{c^2_e(a_\star) - \varepsilon}{\varepsilon}\right)^2 W, & c^2_e(a_\star) > \varepsilon, \end{cases} \tag{40}$$

where $a_\star = (1+1100)^{-1}$, $\varepsilon = 10^{-3}$, $W = 10^4$, and the wall prior penalizes approaching $c^2_e \to 1$ (where the effective Planck mass $M^2_* \propto 1 - c^2_e$ would vanish) over the redshift range of the data,

$$\chi^2_{\rm wall} = \begin{cases} 0, & \max\limits_{a\in[a_{\rm min},1]} c^2_e(a) \le c^2_{\rm wall}, \\ W_{\rm wall}\left(\max c^2_e - c^2_{\rm wall}\right)^2, & \text{otherwise}, \end{cases} \tag{41}$$

with $a_{\rm min} = (1+z_{\rm max})^{-1}$ and $z_{\rm max}$ being the largest redshift used in the likelihood.

Finally, in anchored analysis we impose an external Gaussian prior on the effective Hubble scale $H_0^{\rm eff}$, not on H_0,

$$\chi^2_{H_0^{\rm eff}} = \left(\frac{H_0^{\rm eff} - H_{0,\star}^{\rm eff}}{\sigma_{H_0^{\rm eff}}}\right)^2, \qquad H_0^{\rm eff} = \frac{H_0}{\sqrt{1 - c^2_{e0}}}. \tag{42}$$

This prior is not used to infer the Hubble scale from low-z probes alone. Rather, it enables a consistency test: we ask whether HEED can accommodate a locally inferred high late-time expansion rate while remaining compatible with SN, BAO, CC, and RSD constraints that jointly probe distances and growth.

We sample the posterior $\mathcal{P}(\boldsymbol{\theta} \mid \mathbf{d})$ using the affine-invariant ensemble sampler `emcee` [126], and compute marginalized constraints and triangle plots using `GetDist` [127].

For a simple model-comparison diagnostic, we quote the Akaike and Bayesian information criteria [128–131],

$$\mathrm{AIC} = \chi^2_{\min} + 2N_{\mathrm{par}}, \qquad \mathrm{BIC} = \chi^2_{\min} + N_{\mathrm{par}} \ln N_{\mathrm{data}}, \tag{43}$$

where N_{par} is the number of fitted parameters, and N_{data} is the number of data points entering the simplified likelihood. We report ΔAIC and ΔBIC relative to the corresponding ΛCDM fit. Since the likelihood used here neglects some covariance matrices, these values should be interpreted as indicative rather than as a final Bayesian model selection result. The numerical results of the consistency analysis are collected in Tables 1 and 2. Table 1 reports the adopted priors, marginalized constraints, and best-fit values for the HEED parameters, while Table 2 gives the data set by data set χ^2 contributions and the corresponding $\Delta\chi^2$, AIC and BIC comparison with ΛCDM. These model-comparison indicators are computed within the simplified diagonal likelihood and should therefore be regarded as indicative rather than definitive.

Table 1. Summary of priors, marginalized constraints, and best-fit values for the HEED analysis. The quoted intervals correspond to the marginalized 68% credible ranges. Approximate marginalized constraints read from the one-dimensional posterior marginals in Figure 3.

Parameter	Prior	Marginalized Constraint
H_0^{eff} [km s^{-1} Mpc^{-1}]	external Gaussian anchor	$\simeq 73.0 \pm 1.0$
Ω_m	–	$0.365^{+0.057}_{-0.026}$
c^2_{e0}	$0 \le c^2_{e0} < 1$	$0.16^{+0.19}_{-0.07}$
a_t	late-time activation prior	$0.47^{+0.10}_{-0.13}$
k	$k > 0$	$5.8^{+9.6}_{-3.8}$
σ_8	weak Gaussian prior	$0.779^{+0.045}_{-0.021}$

Table 2. Goodness of fit and information criterion comparison between HEED and ΛCDM. The values are computed with the simplified diagonal likelihood used in this work and should therefore be interpreted as indicative.

Model	χ^2_{SN}	χ^2_{BAO}	χ^2_{CC}	χ^2_{RSD}	χ^2_{tot}	AIC	BIC
ΛCDM	750	21.6	14.7	32.5	819	825	842
HEED	745	19.2	15.1	32.1	811	823	856
HEED $-\Lambda$CDM	-5	-2.4	0.4	-0.4	$\Delta\chi^2 = -8$	$\Delta\mathrm{AIC} = -2$	$\Delta\mathrm{BIC} = 14$

The HEED model, as indicated in Table 2, reduces the total data chi-square by $\Delta\chi^2_{\mathrm{tot}} \simeq -8$. This improvement is driven mainly by the supernova and BAO contributions, $\Delta\chi^2_{\mathrm{SN}} \simeq -5.0$, $\Delta\chi^2_{\mathrm{BAO}} \simeq -2.4$, whereas the changes in the CC and RSD sectors are small, $\Delta\chi^2_{\mathrm{CC}} \simeq +0.4$, $\Delta\chi^2_{\mathrm{RSD}} \simeq -0.4$. Thus, the raw goodness of fit is mildly improved relative to ΛCDM. However, HEED contains three additional free parameters relative to ΛCDM. The corresponding AIC difference is

$$\Delta\mathrm{AIC} \equiv \mathrm{AIC}_{\mathrm{HEED}} - \mathrm{AIC}_{\Lambda\mathrm{CDM}} = \Delta\chi^2_{\mathrm{tot}} + 2\Delta N_{\mathrm{par}} \simeq -8 + 2 \times 3 \simeq -2.$$

A negative value of ΔAIC indicates that the improvement in χ^2 only mildly compensates for the additional HEED parameters. In contrast, the BIC difference is

$$\Delta\mathrm{BIC} \equiv \mathrm{BIC}_{\mathrm{HEED}} - \mathrm{BIC}_{\Lambda\mathrm{CDM}} = \Delta\chi^2_{\mathrm{tot}} + \Delta N_{\mathrm{par}} \ln N_{\mathrm{data}} \simeq -8 + 3\ln(1819) \simeq 14.$$

The positive value of ΔBIC favors ΛCDM, reflecting the stronger BIC penalty for additional parameters when the number of data points is large. We therefore interpret the fit as

an indicative improvement in raw goodness of fit, but not as a robust model selection preference for HEED.

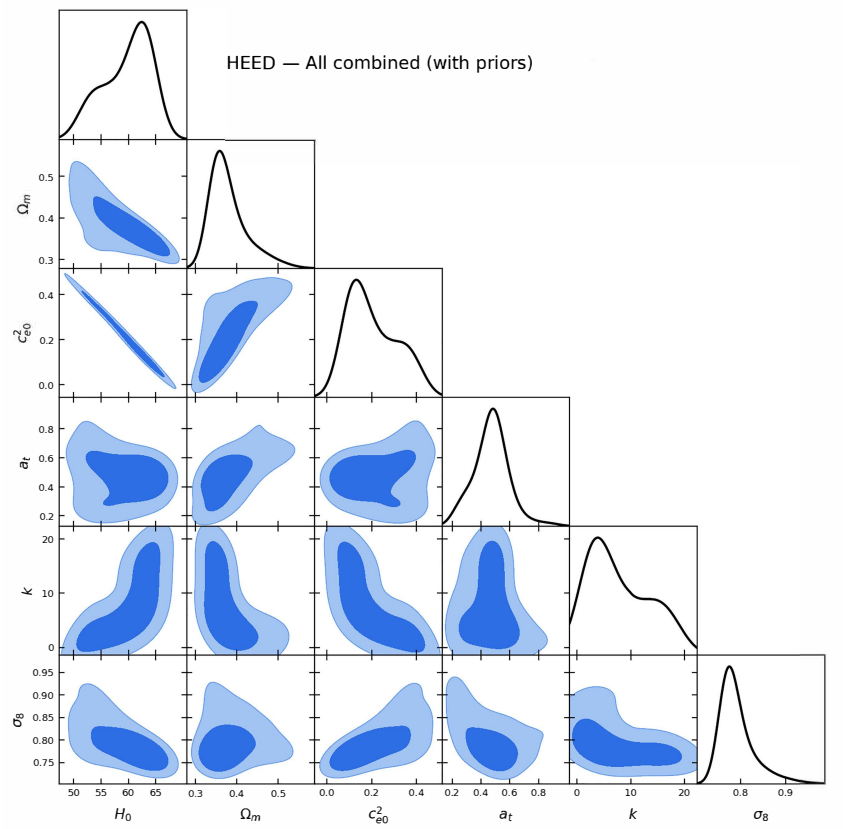


Figure 3. Triangle plot for the HEED parameterization showing the marginalized posterior distributions of $\{H_0, \Omega_m, c^2_{e0}, a_t, k, \sigma_8\}$ obtained from the joint SN + BAO + CC + RSD likelihood. Shaded contours indicate the 68% and 95% credible regions, while the diagonal panels show the corresponding one-dimensional marginals. In the anchored analysis, the external Gaussian prior is applied to the effective late-time Hubble scale $H_0^{\rm eff} = H_0/\sqrt{1 - c^2_{e0}}$ rather than directly to H_0, which induces the characteristic degeneracy direction in the (H_0, c^2_{e0}) plane.

The likelihood adopted in this exploratory analysis treats the compressed SN, BAO, CC, and RSD data points as independent Gaussian measurements. Equivalently, the full covariance expression in Equation (36) is approximated by retaining only the diagonal variances. Neglecting off-diagonal covariances can misestimate both the constraining power of the data and the relative weights of the different data blocks, especially for Pantheon+, correlated BOSS/eBOSS/DESI BAO products, and RSD compilations assembled from partially overlapping galaxy samples.

As a first diagnostic, we repeated the fit including the CC covariance induced by stellar population synthesis systematics, following Ref. [132]. The resulting change in the RSD related fit quality is at the level of approximately 2%. This suggests that the qualitative HEED trends are stable against this particular covariance source. Nevertheless, modern large scale structure (LSS) analyses show that covariance modeling can affect projected uncertainties at the few-percent level. For example, the DESI 2024 covariance validation study of Ref. [133] finds that analytical and mock-based covariance estimates agree well for BAO distance-scale errors, while full shape analyses require a more careful covariance treatment.

Because Pantheon+, BAO, and RSD data products contain non-trivial internal and cross-survey correlations, we conservatively expect a full covariance treatment to affect selected χ^2 contributions and marginalized uncertainties at the few-percent-to-$\mathcal{O}(10\%)$

level. The present diagonal treatment should therefore be regarded as a first consistency test rather than as a definitive quantitative model-selection analysis. A full covariance treatment will be required before claiming a statistical preference for HEED over ΛCDM.

3.2. Posterior Constraints and Internal Consistency of HEED

Figure 3 presents the marginalized one- and two-dimensional posterior distributions for the HEED parameter vector Equation (29), obtained from the joint SN+BAO+CC+RSD likelihood with the priors and profiling procedure specified in Section 3.1. The shaded contours enclose the 68% and 95% credible regions, while the diagonal panels show the corresponding one-dimensional marginals. Complementary to these parameter constraints, the data space fits shown in Figures 4–8 demonstrate that the best-fit HEED and ΛCDM predictions are nearly indistinguishable across the low-redshift observables considered here (Pantheon+ $\mu(z)$, CC $H(z)$, BAO D_M/r_d and D_H/r_d, and RSD $f\sigma_8$), with no systematic preference visible at the level of current uncertainties. We therefore interpret the posterior in Figure 3 primarily as a consistency statement: within the adopted additive HEED embedding and priors, a late-time entanglement-driven modification of the expansion history can be introduced without spoiling established low-z distance and growth constraints.

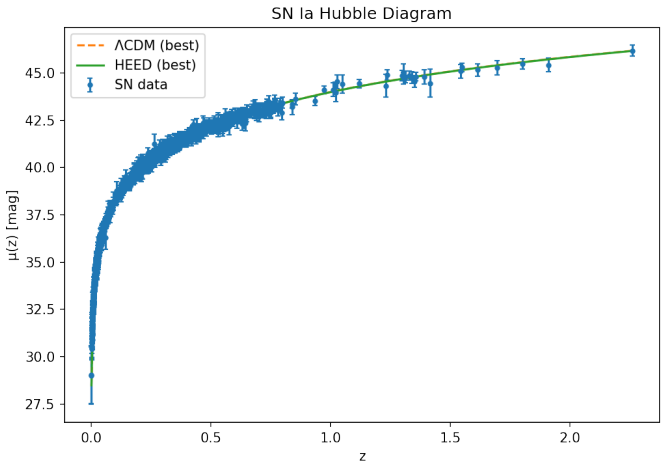


Figure 4. Pantheon+ SN Ia distance moduli $\mu(z)$ compared to the best-fit HEED (solid) and ΛCDM (dashed) predictions. The fits are shown after profiling over the nuisance offset ΔM (absolute-magnitude/zero-point) as described in the text.

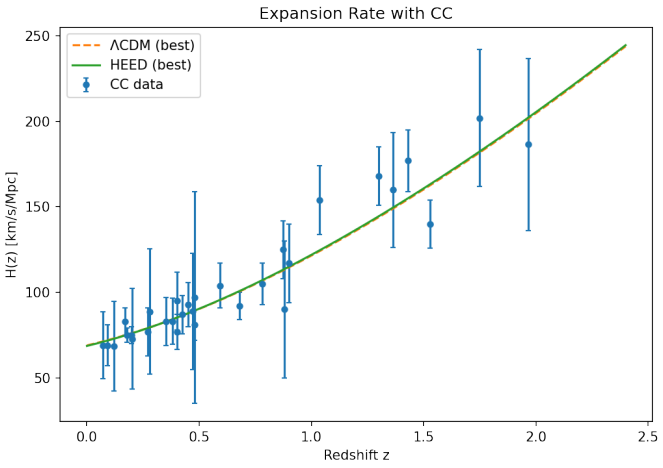


Figure 5. CC measurements of $H(z)$ with 1σ uncertainties compared to the best-fit HEED (solid) and ΛCDM (dashed) predictions.

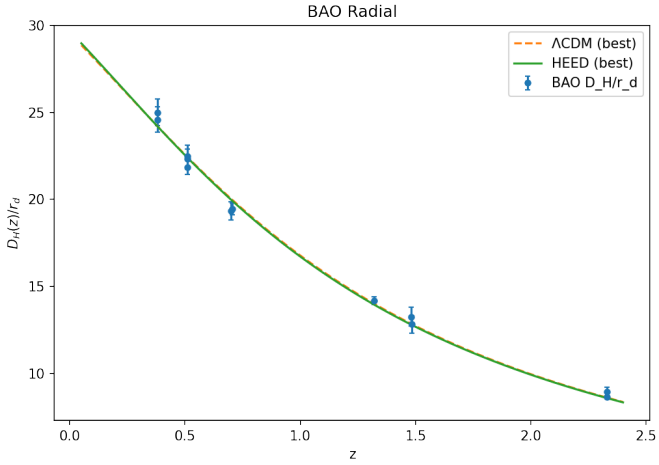


Figure 6. BAO measurements of the radial (line-of-sight) comoving distance, $D_H(z)/r_d$ with $D_H \equiv c/H(z)$, compared to the best-fit HEED (solid) and ΛCDM (dashed) predictions.

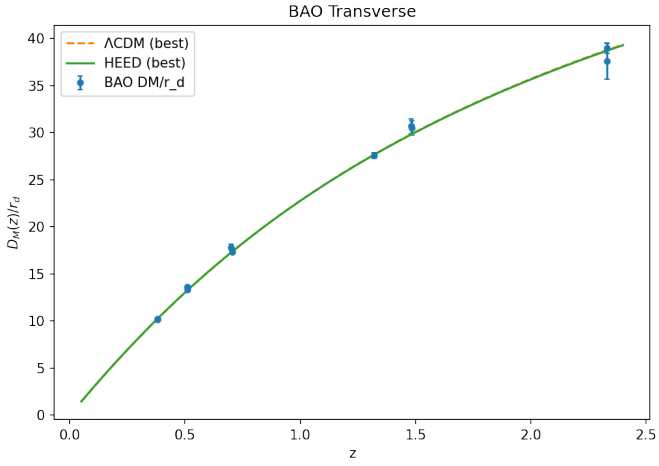


Figure 7. BAO measurements of the transverse comoving distance, $D_M(z)/r_d$, compared to the best-fit HEED (solid) and ΛCDM (dashed) predictions.

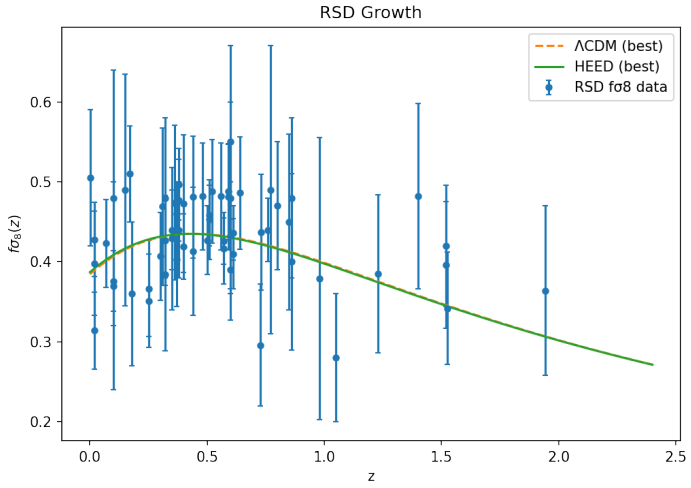


Figure 8. RSD growth constraints in the HEED framework. Measurements of $f\sigma_8(z)$ with 1σ uncertainties compared to the best-fit predictions for HEED (additive embedding) and ΛCDM. Model curves are obtained by solving the linear growth equation Equation (21) assuming a smooth (non-clustering) HEED sector, normalizing $D(a = 1) = 1$, and computing $f\sigma_8(z) = \left(d \ln D / d \ln a\right) \sigma_{8,0}\, D(a)$ at $a = (1+z)^{-1}$.

A number of qualitative and quantitative features demonstrate that the inferred constraints are internally consistent with the physical assumptions underlying HEED.

3.2.1. Hubble Constant

As pointed in Section 3.1, in the present analysis, the posterior is conditioned on an external Gaussian prior ("anchor") on the effective late-time Hubble scale centered at $H_{0,\star}^{\rm eff} = 73\ {\rm km\,s^{-1}\,Mpc^{-1}}$ as inferred from [2]. Accordingly, the chains do not infer an upward shift of the Hubble scale relative to CMB-only analyses; rather, they test whether the HEED background and growth sector can remain compatible with SN + BAO + CC + RSD while accommodating a high locally inferred expansion rate. This is because in the additive HEED embedding Equation (27), the anchor does not force the sampled parameter H_0 itself to be large. Rather, the posterior realizes $H_0^{\rm eff} \simeq 73\ {\rm km\,s^{-1}\,Mpc^{-1}}$ with moderate values of H_0 provided $c_{e0}^2 > 0$, leading to a pronounced anti-correlation between H_0 and c_{e0}^2 in the marginalized posterior shown in Figure 3.

3.2.2. Matter Density

The matter density parameter Ω_m is constrained at the level typical of low-redshift analyses, with a clear anti-correlation with H_0. This degeneracy is expected: an increase in the late-time expansion rate induced by HEED must be compensated by a corresponding adjustment in Ω_m in order to preserve the BAO distance measurements. The inferred values of the matter density parameter remain within the range allowed by late-time LSS probes, including BAO geometry, RSD measurements, and galaxy clustering with weak lensing combinations. In particular, the moderate increase in Ω_m relative to ΛCDM is compensated by the HEED-induced suppression of late-time growth, so that the predicted $f\sigma_8(z)$ remains consistent with current observational constraints.

3.2.3. Present-Day HEED Amplitude

A central result of the analysis is that the posterior for the HEED amplitude c_{e0}^2 peaks decisively away from zero. Pure ΛCDM, corresponding to $c_{e0}^2 = 0$, lies in the tail of the posterior. At the same time, the data strongly disfavor values approaching the physical wall $c_e^2 \to 1$, ensuring a positive effective Planck mass $M_*^2 \propto 1 - c_e^2$ and the absence of instabilities. This provides direct phenomenological support for a nonvanishing late-time horizon entanglement deficit.

3.2.4. Activation Epoch and Sharpness

The activation scale factor a_t is constrained to lie in the range $a_t \sim 0.4-0.6$, corresponding to a redshift $z_t \sim 0.7-1.5$. This places the onset of HEED squarely in the late universe, well after recombination and the baryon-drag epoch. As a result, early universe observables such as the sound horizon remain unaffected, while the late-time expansion history is modified in precisely the redshift range probed by SN, BAO, and CC data.

The shape parameter k, which controls the sharpness of the HEED switch-on, is only weakly constrained by current data and exhibits broad, possibly multi-modal posteriors. This behavior is expected: existing low-redshift probes are primarily sensitive to the integrated effect of the late-time expansion rate rather than to the detailed functional form of the transition. Consequently, k effectively plays the role of a nuisance parameter at present precision.

The weak constraints on the activation parameters (a_t, k) have a simple origin. The data used here are mostly sensitive to the integrated impact of the HEED sector on distances and growth, rather than to the detailed time profile of the transition. Schematically, the activation history enters through $c_e^2(a) = c_{e0}^2\, g(a; a_t, k)$, but SN and BAO observables depend mainly on integrals of the form $D(z) \sim \int_0^z \frac{dz'}{H(z')}$, while RSD measurements constrain combi-

nations such as $f\sigma_8(z)$ that also respond to the cumulative expansion history. Consequently, different pairs (a_t, k) can generate nearly the same integrated distance and growth response once c_{e0}^2, H_0, and Ω_m are adjusted. The parameter a_t is therefore constrained mainly by the requirement that HEED remain inactive before recombination and the baryon-drag epoch, while the sharpness parameter k remains only weakly determined by present low-redshift data. More direct constraints on the transition profile would require observables with finer redshift resolution or additional probes of late-time potentials, such as weak lensing, CMB lensing, or ISW cross-correlations.

3.2.5. Growth Amplitude

The posterior for σ_8 is mildly shifted toward lower values compared to the Planck ΛCDM determination [1]. This reflects the fact that the enhanced late-time expansion induced by HEED leads to a modest suppression of structure growth at $z \lesssim 1$. The resulting values of σ_8 and the correlated predictions for $f\sigma_8(z)$ remain compatible with RSD measurements, while potentially easing the weak-lensing clustering-amplitude (S_8) tension, i.e., the preference of several stage-III cosmic-shear analyses for $S_8 \equiv \sigma_8\sqrt{\Omega_m/0.3}$ values lower than the CMB-inferred Planck ΛCDM prediction (e.g., KiDS-1000 and DES Y3) [134–136].

3.2.6. Correlation Structure

The two-dimensional marginalized posteriors exhibit a pattern of correlations that can be understood directly from the structure of the HEED background and from the combination of the low-redshift probes employed. Because the analysis is conditioned on an external prior on the effective late-time Hubble scale $H_0^{\rm eff}$, the sampled parameters H_0 and c_{e0}^2 are strongly anti-correlated. This follows from the additive HEED relation Equation (27): for a fixed $H_0^{\rm eff}$, a larger entanglement deficit requires a smaller underlying H_0. The corresponding elongated contours in the (H_0, c_{e0}^2) plane therefore reflect a purely kinematic degeneracy rather than a physical instability.

A positive correlation is observed between c_{e0}^2 and Ω_m. In the anchored analysis, increasing c_{e0}^2 lowers the sampled value of H_0, which tends to increase comoving distances at fixed dimensionless expansion rate. To preserve the BAO and CC constraints on distances and $H(z)$, the fit compensates by increasing Ω_m, which raises $Q(z)$ at intermediate redshifts and reduces the integrated distances. This correlation therefore encodes the geometric balance required to maintain consistency with BAO measurements in the presence of a late-time entanglement contribution.

The correlation between c_{e0}^2 and σ_8 reflects the expansion–growth interplay probed by RSDs. A larger entanglement deficit enhances the late-time expansion rate, which mildly suppresses the growth of linear perturbations at $z \lesssim 1$. This suppression can be partially offset by a correlated adjustment of the present-day fluctuation amplitude σ_8, ensuring that the predicted $f\sigma_8(z)$ remains compatible with RSD data. As a result, the joint posterior occupies a region in parameter space where background expansion and structure growth are simultaneously consistent.

Finally, the activation parameters (a_t, k) exhibit broad degeneracies with c_{e0}^2 and with each other. Current low-redshift data primarily constrain the integrated effect of the HEED contribution on the expansion history rather than the detailed time profile of its onset. Consequently, the sharpness parameter k is only weakly constrained, while the activation epoch a_t is restricted to late times by the requirement of early universe safety.

3.2.7. Fits

For the parameter values favored by Figure 3, the best-fit HEED and ΛCDM curves in Figures 4–8 are nearly indistinguishable within the current observational un-

certainties. This behavior is expected. First, the low-redshift data blocks employed here—SN Ia distance moduli, compressed BAO distances, CC $H(z)$ points, and RSD $f\sigma_8(z)$ measurements—primarily constrain integrated distance and expansion combinations and therefore admit substantial degeneracies among late-time expansion histories. In this regime, distinct parameterizations can map onto very similar $H(z)$ and distance predictions once their parameters are adjusted to satisfy the same geometric constraints. Second, our SN likelihood profiles over the nuisance offset ΔM, so SN data constrain relative distances and provide only weak leverage on the absolute expansion scale. Finally, in anchored analyses the external Gaussian prior is applied to the effective late-time Hubble scale $H_0^{\rm eff}$ rather than directly to H_0. Consequently, the parameters H_0 and c_{e0}^2 can trade off along the degeneracy direction implied by the additive HEED embedding while keeping $H_0^{\rm eff}$ (and hence much of the low-z expansion history) close to the anchored value. The close overlap of the corresponding best-fit curves thus indicates that HEED can accommodate a nonzero late-time entanglement amplitude without spoiling established low-z distance and growth constraints, while also highlighting that present data have limited power to distinguish HEED from ΛCDM at the level of background and linear growth observables.

3.2.8. Implications

Taken together, the posterior distributions demonstrate that HEED operates in the regime it was designed for: it activates only at late times, modifies the expansion history at the few-percent level, preserves early universe physics, and remains consistent with structure–growth constraints. While the current data do not yet yield a statistically decisive preference over ΛCDM, the results show that HEED can significantly alleviate the Hubble tension without introducing pathologies or fine-tuning, and they motivate further tests with upcoming LSS and CMB–LSS cross-correlation data. These results should therefore be interpreted as an anchored consistency test (high $H_0^{\rm eff}$ imposed), rather than as a free, low-z determination of the Hubble scale.

4. Conclusions

We have developed and confronted a simple realization of HEED as a late-time, IR contribution to the cosmic energy budget. In HEED, the apparent (Hubble) horizon acts as an entanglement screen whose quantum correlations do not fully saturate the Bekenstein–Hawking entropy at late times. The resulting deficit is mapped, via horizon thermodynamics and equipartition, into a smooth bulk component whose characteristic scaling is $\rho_{\rm HEED} \propto H^2/G$. This scaling is of precisely the magnitude required to affect late-time expansion while remaining negligible at recombination, and it is qualitatively distinct from free-field vacuum effects that generate parametrically smaller $\delta\rho \sim H^4$ corrections.

At the level of internal consistency, HEED is compatible with standard requirements of cosmological model building. In the additive embedding used throughout this work, the entanglement sector modifies the background through an algebraic rescaling of the Friedmann equation while preserving the Bianchi identity and covariant conservation of matter, $\dot\rho_m + 3H\rho_m = 0$. By construction the model remains physical provided $0 \le c_e^2(a) < 1$, which ensures a positive effective Planck mass $M_*^2 \propto 1 - c_e^2$ and avoids the pathologies associated with vanishing gravitational coupling. Interpreted as an effective, nonpropagating IR sector, HEED can transiently realize an effective equation of state below -1 during its switch on without implying ghost instabilities, since no additional propagating degree of freedom is introduced.

Phenomenologically, HEED is predictive and testable. The characteristic late-time activation yields a few-percent upward shift of the effective Hubble scale, modifies dis-

tances at $z \lesssim \mathcal{O}(1)$, and produces a mild suppression of linear growth together with a modest enhancement of the late, integrated Sachs–Wolfe (ISW) effect. Importantly, the best-fit HEED and ΛCDM curves across the low-redshift observables considered (SN Ia, BAO, CC, and RSD) are nearly indistinguishable within current uncertainties, indicating that the HEED mechanism can be switched on at late times without spoiling established distance and growth constraints. This near degeneracy also emphasizes that robust discrimination will require either higher-precision low-z measurements, additional growth probes (e.g., weak lensing and CMB lensing) [134,135,137–139], or may require CMB–LSS cross correlations that directly probe the late-time ISW response, through temperature–tracer correlations and related estimators [140–145]. Although ISW measurements are not considered in the present study, this effect offers an additional, in-principle-observable lever for distinguishing HEED from purely geometric modifications.

The present analysis should therefore be interpreted as an anchored low-redshift consistency test, not as a definitive demonstration that the Hubble tension is resolved. The likelihood includes an external Gaussian anchor on the effective late-time Hubble scale $H_0^{\rm eff}$, so the posterior does not represent a free inference of a high H_0 from SN + BAO + CC + RSD data alone. Rather, given a high local expansion scale, we test whether the HEED activation sector can accommodate it without significantly degrading the fit to current distance and growth observables. In this sense, the terms "alleviate" and "accommodate" are used conditionally throughout this paper, and should not be interpreted as a claim of a statistically established resolution of the Hubble tension.

Finally, we stress the conceptual advantage of anchoring the IR contribution to a quasi-local horizon. Teleological issues refer to pathologies that arise when present-time quantities depend on the entire future history of the universe. The future event horizon is a global object: its existence and radius at time t depend on whether signals emitted after t will ever reach the observer, which requires knowledge of the spacetime to arbitrarily late times. Consequently, models that set an IR cutoff by the future event horizon make the present energy density a functional of the future expansion history, leading to acausality and nonlocal in-time evolution. In contrast, the apparent (Hubble) horizon in FLRW is determined quasi-locally on each time slice and underlies local horizon thermodynamics and derivations of the Friedmann equations via first-law equipartition arguments. HEED ties its IR contribution to the apparent (Hubble) horizon and therefore remains local in time, avoiding the teleology inherent to future event horizon models [42,46,49,86].

Several extensions are immediate. A next step is a full-model comparison with ΛCDM using consistent covariances for SN and BAO products and including additional growth information (cosmic shear, CMB lensing, and cluster abundance). On the theory side, the HEED parameterization can be sharpened by constructing microphysical models for the deficit function $\delta(a)$ (or $c_e^2(a)$), e.g., in terms of horizon mutual information, entanglement–wedge capacity, or Gauss law constraints on gravitational dressing. These developments would move HEED from a phenomenological IR mechanism toward a predictive, first-principles account of how horizon entanglement can influence late-time cosmology.

A central limitation of the present analysis is that HEED is formulated here as an effective FLRW-level description and not yet derived from a fully covariant microscopic bulk theory. Establishing such an underpinning, or deriving the activation function from first principles, remains an important problem for future work. Accordingly, the significance of the present work is not that it supplies a complete fundamental theory, but that it identifies a concrete IR mechanism, motivated by horizon thermodynamics, whose background and growth signatures can be tested directly against cosmological observations.

Author Contributions: Conceptualization, A.S.S., R.K. and M.G.; methodology, A.S.S. and R.K.; software, R.K., A.S.S. and J.S.; validation, A.S.S., R.K., M.G. and J.S.; formal analysis, A.S.S., R.K., M.G. and J.S.; text writing A.S.S., R.K. and M.G. All authors have read and agreed to the published version of this manuscript.

Funding: The work of R.K. and J.S. was partially supported by the Kakos Endowed Chair in Science Fellowship.

Data Availability Statement: The CC, BAO, and RSD data sets used in this analysis are publicly available and are reported in Tables A1, A2, and A3, respectively, with the corresponding references attributed to each data point. The likelihoods described in Section 3 were sampled using the publicly available `emcee` package [126], while posterior processing and visualization were carried out with `GetDist` [127]. Requests concerning the analysis-specific likelihood implementation may be addressed to the corresponding author.

Conflicts of Interest: The authors declare no conflicts of interest.

Abbreviations

The following abbreviations are used in this manuscript:

2dFGRS	2-degree Field Galaxy Redshift Survey
2MRS	2MASS Redshift Survey
2MTF	2MASS Tully–Fisher Survey
6dFGS	6-degree Field Galaxy Survey
ACT	Atacama Cosmology Telescope
BAO	Baryon acoustic oscillations
BH	Bekenstein–Hawking
BOSS	Baryon Oscillation Spectroscopic Survey
CC	Cosmic chronometer
CDM	Cold dark matter
CFT	Conformal field theory
CMB	Cosmic microwave background
CMASS	Constant-mass galaxy sample
DA	Differential age
DES	Dark Energy Survey
DESI	Dark Energy Spectroscopic Instrument
DR	Data release
eBOSS	Extended Baryon Oscillation Spectroscopic Survey
EDE	Early dark energy
EFT	Effective field theory
FLRW	Friedmann–Lemaître–Robertson–Walker
GAMA	Galaxy And Mass Assembly
GR	General relativity
HDE	Holographic dark energy
HEED	Horizon entanglement equipartition deficit
HSC	Hyper Suprime-Cam
IR	Infrared
IRAS	Infrared Astronomical Satellite
ISW	Integrated Sachs–Wolfe
KiDS	Kilo-Degree Survey
LOWZ	Low-redshift galaxy sample
LRG	Luminous red galaxy
LSS	Large-scale structure
MGS	Main galaxy sample
ODE	Ordinary differential equation
PDR	Public data release

QFT	Quantum field theory
QSO	Quasar
RSD	Redshift-space distortions
SDSS	Sloan Digital Sky Survey
SH0ES	Supernovae, H_0, for the Equation of State of Dark Energy
SN	Supernova
SNe	Supernovae
SN Ia	Type Ia supernova
UV	Ultraviolet
VIPERS	VIMOS Public Extragalactic Redshift Survey
VVDS	VIMOS VLT Deep Survey
ΛCDM	Lambda cold dark matter

Appendix A. Entanglement First Law, Modular Energy, and the H^4 Scaling

Consider a quantum field theory (beginning with a free/conformal scalar) in $3+1$ dimensions on a spatial slice of a FLRW spacetime that is close to de Sitter with Hubble parameter H. Let B be a ball of radius R (possibly of order the Hubble radius) on a constant–time slice. For a conformal field theory (CFT) in flat space, the vacuum modular Hamiltonian $\mathcal{H}_B$ for a ball is local and can be written as

$$\mathcal{H}_B = 2\pi \int_B d^3x \, \frac{R^2 - r^2}{2R} \, T_{00}(x) + \text{const.}, \tag{A1}$$

as obtained from the conformal map between the ball and a hyperbolic/Rindler wedge [80,81].

The first law of entanglement states that for small state/geometry variations

$$\delta S_B = \delta \langle \mathcal{H}_B \rangle = 2\pi \int_B d^3x \, \frac{R^2 - r^2}{2R} \, \delta \langle T_{00}(x) \rangle, \tag{A2}$$

which is the linearized relation between entanglement entropy and modular energy (relative entropy at first order) [82,83].

In a smooth curved background, the renormalized vacuum stress tensor of a four-dimensional CFT is controlled by the conformal (trace) anomaly; therefore, in de Sitter (Weyl-flat with $C_{\mu\nu\rho\sigma} = 0$) one has

$$\langle T_{\mu\nu} \rangle_{\text{vac}} = c_A \, H^4 \, g_{\mu\nu}, \tag{A3}$$

with c_A fixed by the type-A anomaly and field content [84]. Dimensional analysis in 4D implies $\langle T_{\mu\nu} \rangle \propto H^4$ in the IR. For a small deformation from Minkowski/adiabatic vacuum to (quasi) de Sitter,

$$\delta \langle T_{00} \rangle \sim \sigma \, H^4, \tag{A4}$$

where σ is a dimensionless coefficient set by field content.

Using the spherical weight and

$$\int_0^R 4\pi r^2 (R^2 - r^2) \, dr = \frac{8\pi}{15} R^5,$$

Equation (A2) gives

$$\begin{aligned} \delta S_B &= 2\pi \, \frac{1}{2R} \, \delta \langle T_{00} \rangle \int_B d^3x \, (R^2 - r^2) \\ &= \frac{8\pi^2}{15} \, R^4 \, \delta \langle T_{00} \rangle \sim \frac{8\pi^2}{15} \, R^4 \, \sigma \, H^4. \end{aligned} \tag{A5}$$

For a ball in a CFT vacuum, the modular (entanglement) temperature is $T_{\rm mod} = 1/(2\pi R)$. A Clausius-like relation then yields

$$\delta E_B = T_{\rm mod}\,\delta S_B = \frac{1}{2\pi R}\cdot\frac{8\pi^2}{15}R^4\,\delta\langle T_{00}\rangle = \frac{4\pi}{15}\,R^3\,\delta\langle T_{00}\rangle, \tag{A6}$$

and dividing by the ball volume $V_B = (4\pi/3)R^3$ gives the renormalized energy-density shift

$$\delta\rho = \frac{\delta E_B}{V_B} = \frac{1}{5}\,\delta\langle T_{00}\rangle \sim \mathcal{O}(H^4). \tag{A7}$$

Thus, free/CFT vacuum contributions to the late-time energy density scale as H^4 and are negligible compared to the critical density $\rho_{\rm crit} = 3H^2/(8\pi G)$:

$$\frac{\delta\rho}{\rho_{\rm crit}} \sim \left(\frac{H}{M_{\rm Pl}}\right)^2 \ll 1. \tag{A8}$$

A careful modular Hamiltonian first-law analysis shows that standard free-field entanglement yields only $\mathcal{O}(H^4)$ energy density corrections at late times. Hence, any phenomenologically relevant $\sim H^2/G$ component must arise from IR/holographic or nonlocal/emergent physics tied to the horizon scale, not from the UV area law of free fields.

The H^4 scaling derived above concerns the finite, renormalized, state-dependent IR response of free/CFT fields to a smooth (quasi–)de Sitter background, for which the only available macroscopic scale is H, and thus $\delta\langle T_{\mu\nu}\rangle \propto H^4 g_{\mu\nu}$. By contrast, the UV part of vacuum entanglement across a smooth surface produces a nonuniversal area-law divergence, $S_{\rm ent} \sim \eta\, A/\epsilon^2$, where ϵ is a short-distance regulator (UV cutoff), and η depends on field content and the scheme. In semiclassical gravity, the same UV modes renormalize the Einstein–Hilbert coupling (and higher-curvature terms), so that the geometric entropy is expressed in terms of the renormalized Newton constant $G_{\rm ren}$, and the UV area term is not an additional dynamical component [56,57,85]. Counting the area law again as an energy density would therefore double count degrees of freedom already absorbed into $G_{\rm ren}$. Consequently, free-field entanglement does not generate a late-time $\mathcal{O}(H^2/G)$ contribution: light fields continue to give $\mathcal{O}(H^4)$ IR effects, while heavy fields mainly renormalize local couplings.

Appendix B. Data

Table A1. CC $H(z)$ measurements (classic 31-point, typically treated as non-correlated). Uncertainties are 1σ.

z	$H(z)$ [km s^{-1} Mpc^{-1}]	σ [km s^{-1} Mpc^{-1}]	Refs.	Year
0.07	69.0	19.6	[88]	2014
0.09	69.0	12.0	[89]	2005
0.12	68.6	26.2	[88]	2014
0.17	83.0	8.0	[89]	2005
0.179	75.0	4.0	[90]	2012
0.199	75.0	5.0	[90]	2012
0.200	72.9	29.6	[88]	2014
0.270	77.0	14.0	[89]	2005
0.280	88.8	36.6	[88]	2014
0.352	83.0	14.0	[90]	2012
0.3802	83.0	13.5	[91]	2016

Table A1. *Cont.*

z	$H(z)$ [km s^{-1} Mpc^{-1}]	σ [km s^{-1} Mpc^{-1}]	Refs.	Year
0.400	95.0	17.0	[89]	2005
0.4004	77.0	10.2	[91]	2016
0.4247	87.1	11.2	[91]	2016
0.4497	92.8	12.9	[91]	2016
0.470	89.0	34.0	[93]	2017
0.4783	80.9	9.0	[91]	2016
0.480	97.0	62.0	[94]	2010
0.593	104.0	13.0	[90]	2012
0.680	92.0	8.0	[90]	2012
0.781	105.0	12.0	[90]	2012
0.875	125.0	17.0	[90]	2012
0.880	90.0	40.0	[94]	2010
0.900	117.0	23.0	[89]	2005
1.037	154.0	20.0	[90]	2012
1.300	168.0	17.0	[89]	2005
1.363	160.0	33.6	[92]	2015
1.430	177.0	18.0	[89]	2005
1.530	140.0	14.0	[89]	2005
1.750	202.0	40.0	[89]	2005
1.965	186.5	50.4	[92]	2015

Table A2. BAO transverse comoving and radial (Hubble) distance measurements, shown jointly as $D_M(z)/r_d$ and $D_H(z)/r_d$ with 1σ uncertainties. Numerical values are taken from Table 4 of Ref. [13], Table III of Ref. [14] and Table IV of Ref. [4]. BOSS/eBOSS BAO data are also summarized in Ref. [146].

z	D_M/r_d	σ_{D_M/r_d}	D_H/r_d	σ_{D_H/r_d}	Refs.	Year
0.38	10.23	0.17	25.00	0.76	[14]	2020
0.38	10.16	0.18	24.59	0.72	[13]	2016
0.51	13.588	0.167	21.863	0.425	[4]	2025
0.51	13.36	0.21	22.33	0.58	[14]	2020
0.51	13.6	0.2	22.49	0.62	[13]	2016
0.70	17.86	0.33	19.33	0.53	[14]	2020
0.706	17.351	0.177	19.455	0.33	[4]	2025
1.321	27.601	0.318	14.176	0.221	[4]	2025
1.48	30.69	0.80	13.26	0.55	[14]	2020
1.484	30.512	0.76	12.817	0.516	[4]	2025
2.33	38.988	0.531	8.632	0.101	[4]	2025
2.33	37.6	1.9	8.93	0.28	[14]	2020

Table A3. RSD growth rate measurements $f\sigma_8(z)$ and 1σ uncertainties. Data acquired from Table II of Ref. [117].

Index	Dataset	z	$f\sigma_8(z)$	Refs.	Year
1	SDSS-LRG	0.35	0.440 ± 0.050	[118]	2006
2	VVDS	0.77	0.490 ± 0.180	[118]	2009
3	2dFGRS	0.17	0.510 ± 0.060	[118]	2009
4	2MRS	0.02	0.314 ± 0.048	[109,110]	2010
5	SnIa+IRAS	0.02	0.398 ± 0.065	[110,147]	2011
6	SDSS-LRG-200	0.25	0.3512 ± 0.0583	[119]	2011
7	SDSS-LRG-200	0.37	0.4602 ± 0.0378	[119]	2011
8	SDSS-LRG-60	0.25	0.3665 ± 0.0601	[119]	2011
9	SDSS-LRG-60	0.37	0.4031 ± 0.0586	[119]	2011
10	WiggleZ	0.44	0.413 ± 0.080	[101]	2012

Table A3. *Cont.*

Index	Dataset	z	$f\sigma_8(z)$	Refs.	Year
11	WiggleZ	0.60	0.390 ± 0.063	[101]	2012
12	WiggleZ	0.73	0.437 ± 0.072	[101]	2012
13	6dFGS	0.067	0.423 ± 0.055	[111]	2012
14	SDSS-BOSS	0.30	0.407 ± 0.055	[100]	2012
15	SDSS-BOSS	0.40	0.419 ± 0.041	[100]	2012
16	SDSS-BOSS	0.50	0.427 ± 0.043	[100]	2012
17	SDSS-BOSS	0.60	0.433 ± 0.067	[100]	2012
18	Vipers	0.80	0.470 ± 0.080	[102]	2013
19	SDSS-DR7-LRG	0.35	0.429 ± 0.089	[120]	2013
20	GAMA	0.18	0.360 ± 0.090	[124]	2013
21	GAMA	0.38	0.440 ± 0.060	[124]	2013
22	BOSS-LOWZ	0.32	0.384 ± 0.095	[95]	2013
23	SDSS DR10 and DR11	0.32	0.480 ± 0.100	[95]	2013
24	SDSS DR10 and DR11	0.57	0.417 ± 0.045	[95]	2013
25	SDSS-MGS	0.15	0.490 ± 0.145	[121]	2015
26	SDSS-veloc	0.10	0.370 ± 0.130	[122]	2015
27	FastSound	1.40	0.482 ± 0.116	[113]	2015
28	SDSS-CMASS	0.59	0.488 ± 0.060	[97]	2016
29	BOSS DR12	0.38	0.497 ± 0.045	[13]	2016
30	BOSS DR12	0.51	0.458 ± 0.038	[13]	2016
31	BOSS DR12	0.61	0.436 ± 0.034	[13]	2016
32	BOSS DR12	0.38	0.477 ± 0.051	[98]	2016
33	BOSS DR12	0.51	0.453 ± 0.050	[98]	2016
34	BOSS DR12	0.61	0.410 ± 0.044	[98]	2016
35	Vipers v7	0.76	0.440 ± 0.040	[103]	2016
36	Vipers v7	1.05	0.280 ± 0.080	[103]	2016
37	BOSS LOWZ	0.32	0.427 ± 0.056	[96]	2016
38	BOSS CMASS	0.57	0.426 ± 0.029	[96]	2016
39	Vipers	0.727	0.296 ± 0.0765	[104]	2016
40	6dFGS+SnIa	0.02	0.428 ± 0.0465	[112]	2016
41	Vipers	0.60	0.480 ± 0.120	[105]	2016
42	Vipers	0.86	0.480 ± 0.100	[105]	2016
43	Vipers PDR-2	0.60	0.550 ± 0.120	[106]	2016
44	Vipers PDR-2	0.86	0.400 ± 0.110	[106]	2016
45	SDSS DR13	0.10	0.480 ± 0.160	[123]	2016
46	2MTF	0.001	0.505 ± 0.085	[108]	2017
47	Vipers PDR-2	0.85	0.450 ± 0.110	[107]	2017
48	BOSS DR12	0.31	0.469 ± 0.098	[99]	2017
49	BOSS DR12	0.36	0.474 ± 0.097	[99]	2017
50	BOSS DR12	0.40	0.473 ± 0.086	[99]	2017
51	BOSS DR12	0.44	0.481 ± 0.076	[99]	2017
52	BOSS DR12	0.48	0.482 ± 0.067	[99]	2017
53	BOSS DR12	0.52	0.488 ± 0.065	[99]	2017
54	BOSS DR12	0.56	0.482 ± 0.067	[99]	2017
55	BOSS DR12	0.59	0.481 ± 0.066	[99]	2017
56	BOSS DR12	0.64	0.486 ± 0.070	[99]	2017
57	SDSS DR7	0.10	0.376 ± 0.038	[125]	2017
58	SDSS-IV	1.52	0.420 ± 0.076	[115]	2018
59	SDSS-IV	1.52	0.396 ± 0.079	[116]	2018
60	SDSS-IV	0.978	0.379 ± 0.176	[114]	2018
61	SDSS-IV	1.23	0.385 ± 0.099	[114]	2018
62	SDSS-IV	1.526	0.342 ± 0.070	[114]	2018
63	SDSS-IV	1.944	0.364 ± 0.106	[114]	2018

Notes

[1] The Planck length is $L_p \equiv \sqrt{\hbar G/c^3}$; in the natural units used here ($\hbar = c = \kappa = 1$), one has $L_p^2 = G$. It sets the area quantum that appears in black hole horizon thermodynamics [43,45].

[2] The twice contracted Bianchi identity $\nabla_\mu G^{\mu\nu} = 0$ is a geometric identity [67,68]. With Einstein's equation $G^{\mu\nu} = 8\pi G\, T^{\mu\nu}$, this implies covariant conservation $\nabla_\mu T^{\mu\nu} = 0$. For a homogeneous fluid component, this yields $\dot{\rho} + 3H(\rho + p) = 0$, and for pressureless matter $\dot{\rho}_m + 3H\rho_m = 0$, as used in the text.

[3] α_T (tensor-speed excess) controls the propagation speed of gravitational waves, $c_T^2 = 1 + \alpha_T$. Low-redshift bounds from GW170817/GRB170817A imply $|\alpha_T| \approx 0$ today [66]. α_B (braiding) quantifies kinetic mixing between the scalar sector and the metric ("kinetic gravity braiding"), modifying the Poisson equation and the metric slip and thus growth/ISW signals [65,74]. α_K (kineticity) measures the normalization of the scalar perturbation's kinetic term in unitary gauge; it affects the scalar sound speed and no-ghost/no-gradient stability conditions but does not directly modify the tensor sector [65,73].

[4] See, e.g., [75–77] for derivations and discussions of linear growth in GR.

References

1. Aghanim, N. et al. [Planck Collaboration]. Planck 2018 results. VI. Cosmological parameters. *Astron. Astrophys.* **2020**, *641*, A6. [CrossRef]
2. Riess, A.G.; Yuan, W.; Macri, L.M.; Scolnic, D.; Brout, D.; Casertano, S.; Jones, D.O.; Murakami, Y.; Anand, G.S.; Breuval, L. ; et al. A comprehensive measurement of the local value of the Hubble constant with 1 km s^{-1} Mpc^{-1} uncertainty from the Hubble Space Telescope and the SH0ES Team. *Astrophys. J. Lett.* **2022**, *934*, L7. [CrossRef]
3. Adame, A.G. et al. [DESI Collaboration]. DESI 2024 VI: Cosmological constraints from the measurements of baryon acoustic oscillations. *J. Cosmol. Astropart. Phys.* **2025**, *2025* , 021. [CrossRef]
4. Abdul Karim, M. et al. [DESI Collaboration]. DESI DR2 results. II. Measurements of baryon acoustic oscillations and cosmological constraints. *Phys. Rev. D* **2025**, *112*, 083515. [CrossRef]
5. Vagnozzi, S. New physics in light of the H_0 tension: An alternative view. *Phys. Rev. D* **2020**, *102*, 023518. [CrossRef]
6. Di Valentino, E.; Mena, O.; Pan, S.; Visinelli, L.; Yang, W.; Melchiorri, A.; Mota, D.F.; Riess, A.G.; Silk, J. In the realm of the Hubble tension: A review of solutions. *Class. Quantum Grav.* **2021**, *38*, 153001. [CrossRef]
7. Abdalla, E.; Abellán, G.F.; Aboubrahim, A.; Agnello, A.; Akarsu, Ö.; Akrami, Y.; Alestas, G.; Aloni, D.; Amendola, L.; Anchordoqui, L.A.; et al. Cosmology intertwined: A review of the particle physics, astrophysics, and cosmology associated with the cosmological tensions and anomalies. *J. High Energy Astrophys.* **2022**, *34*, 49–211 . [CrossRef]
8. Schöneberg, N.; Franco Abellán, G.; Pérez Sánchez, A.; Witte, S.J.; Poulin, V.; Lesgourgues, J. The H0 Olympics: A fair ranking of proposed models. *Phys. Rep.* **2022**, *984*, 1–55. [CrossRef]
9. Vagnozzi, S. Seven hints that early-time new physics alone is not sufficient to solve the Hubble tension. *Universe* **2023**, *9*, 393. [CrossRef]
10. Di Valentino, E. et al. [CosmoVerse Network]. The CosmoVerse White Paper: Addressing observational tensions in cosmology with systematics and fundamental physics. *Phys. Dark Universe* **2025**, *49*, 101965. [CrossRef]
11. Pedrotti, D.; Escamilla, L.A.; Marra, V.; Perivolaropoulos, L.; Vagnozzi, S. BAO miscalibration cannot rescue late-time solutions to the Hubble tension. *Phys. Rev. D* **2026**, *113*, 043507. [CrossRef]
12. Scolnic, D.; Brout, D.; Carr, A.; Riess, A.G.; Davis, T.M.; Dwomoh, A.; Jones, D.O.; Ali, N.; Kenworthy, W.D.; Peterson, E.R.; et al. The Pantheon+ analysis: The full data set and light-curve release. *Astrophys. J.* **2022**, *938*, 113. [CrossRef]
13. Alam, S. et al. [BOSS Collaboration]. The clustering of galaxies in the completed SDSS-III Baryon Oscillation Spectroscopic Survey: Cosmological analysis of the DR12 galaxy sample. *Mon. Not. R. Astron. Soc.* **2017**, *470*, 2617–2652. [CrossRef]
14. Alam, S.; Aubert, M.; Avila, S.; Balland, C.; Bautista, J.E.; Bershady, M.A.; Bizyaev, D.; Blanton, M.R.; Bolton, A.S.; Bovy, J.; et al. Completed SDSS-IV Extended Baryon Oscillation Spectroscopic Survey: Cosmological implications from two decades of spectroscopic surveys at the Apache Point Observatory. *Phys. Rev. D* **2021**, *103*, 083533. [CrossRef]
15. Ivanov, M.M.; McDonough, E.; Hill, J.C.; Simonović, M.; Toomey, M.W.; Alexander, S.; Zaldarriaga, M. Constraining early dark energy with large-scale structure. *Phys. Rev. D* **2020**, *102*, 103502. [CrossRef]
16. Hill, J.C.; Calabrese, E.; Aiola, S.; Battaglia, N.; Bolliet, B.; Choi, S.K.; Devlin, M.J.; Duivenvoorden, A.J.; Dunkley, J.; Ferraro, S.; et al. Atacama Cosmology Telescope: Constraints on prerecombination early dark energy. *Phys. Rev. D* **2022**, *105*, 123536. [CrossRef]
17. Cohen, A.G.; Kaplan, D.B.; Nelson, A.E. Effective field theory, black holes, and the cosmological constant. *Phys. Rev. Lett.* **1999**, *82*, 4971. [CrossRef]
18. Li, M. A model of holographic dark energy. *Phys. Lett. B* **2004**, *603*, 1–5. [CrossRef]
19. Hsu, S.D.H. Entropy bounds and dark energy. *Phys. Lett. B* **2004**, *594*, 13–16. [CrossRef]
20. Wang, S.; Wang, Y.; Li, M. Holographic dark energy. *Phys. Rep.* **2017**, *696*, 1–57. [CrossRef]

21. Doran, M.; Robbers, G.; Wetterich, C. Impact of three years of data from the Wilkinson Microwave Anisotropy Probe on cosmological models with dynamical dark energy. *Phys. Rev. D* **2007**, *75*, 023003. [CrossRef]
22. Caldera-Cabral, G.; Maartens, R.; Ureña-López, L.A. Dynamics of interacting dark energy. *Phys. Rev. D* **2009**, *79*, 063518. [CrossRef]
23. Linder, E.V. Extending the gravitational growth framework. *Phys. Rev. D* **2009**, *79*, 063519. [CrossRef]
24. Hu, W.; Sawicki, I. Models of $f(R)$ cosmic acceleration that evade solar-system tests. *Phys. Rev. D* **2007**, *76*, 064004. [CrossRef]
25. Montani, G.; Escamilla, L.A.; Carlevaro, N.; Di Valentino, E. Decay of $f(R)$ quintessence into dark matter: Mitigating the Hubble tension? *Phys. Rev. D* **2026**, *113*, 023507. [CrossRef]
26. Song, Y.-S.; Hu, W.; Sawicki, I. Large scale structure of $f(R)$ gravity. *Phys. Rev. D* **2007**, *75*, 044004. [CrossRef]
27. Cruz, J.S.; Hannestad, S.; Holm, E.B.; Niedermann, F.; Sloth, M.S.; Tram, T. Profiling cold new early dark energy. *Phys. Rev. D* **2023**, *108*, 023518. [CrossRef]
28. Herold, L.; Ferreira, E.G.M. Resolving the Hubble tension with early dark energy. *Phys. Rev. D* **2023**, *108*, 043513. [CrossRef]
29. Yao, Y.-H.; Wang, J.-C.; Meng, X.-H. Observational constraints on noncold dark matter and phenomenological emergent dark energy. *Phys. Rev. D* **2024**, *109*, 063502. [CrossRef]
30. Pooya, N.N. Growth of matter perturbations in the interacting dark energy–dark matter scenarios. *Phys. Rev. D* **2024**, *110*, 043510. [CrossRef]
31. Chudaykin, A.; Kunz, M. Modified gravity interpretation of the evolving dark energy in light of DESI data. *Phys. Rev. D* **2024**, *110*, 123524. [CrossRef]
32. Escamilla, L.A.; Fiorucci, D.; Montani, G.; Di Valentino, E. Exploring the Hubble tension with a late-time modified gravity scenario. *Phys. Dark Universe* **2024**, *46*, 101652. [CrossRef]
33. Luongo, O.; Pace, F.; Tomasi, S. Linear and nonlinear clusterings of Horndeski-inspired dark energy models with fast transition. *Phys. Rev. D* **2024**, *110*, 083523. [CrossRef]
34. Adil, S.A.; Akarsu, Ö.; Valentino, E.D.; Nunes, R.C.; Özülker, E.; Sen, A.A.; Specogna, E. Omnipotent dark energy: A phenomenological answer to the Hubble tension. *Phys. Rev. D* **2024**, *109*, 023527. [CrossRef]
35. Fazzari, E.; Dainotti, M.G.; Montani, G.; Melchiorri, A. The effective running Hubble constant in SNe Ia as a marker for the dark energy nature. *J. High Energy Astrophys.* **2026**, *49*, 100459. [CrossRef]
36. Montani, G.; Carlevaro, N.; Dainotti, M.G. Running Hubble constant: Evolutionary dark energy. *Phys. Dark Universe* **2025**, *48*, 101847. [CrossRef]
37. Montani, G.; Fazzari, E.; Carlevaro, N.; Dainotti, M.G. Two dynamical scenarios for binned master sample interpretation. *Entropy* **2025**, *27*, 895. [CrossRef] [PubMed]
38. Montani, G.; Carlevaro, N.; Dainotti, M.G. Slow-rolling scalar dynamics as solution for the Hubble tension. *Phys. Dark Universe* **2024**, *44*, 101486. [CrossRef]
39. Carloni, Y.; Luongo, O. A barotropic alternative to Early Dark Energy for alleviating the H_0 tension . *arXiv* **2026**. [CrossRef]
40. Akarsu, Ö.; Perivolaropoulos, L.; Tsikoundoura, A.; Yükselci, A.E.; Zhuk, A. Dynamical dark energy with AdS-to-dS and dS-to-dS transitions: Implications for the H_0 tension . *arXiv* **2025**. [CrossRef]
41. Carloni, Y.; Luongo, O.; Muccino, M. Addressing the H_0 tension through matter with pressure and no early dark energy. *Astron. Astrophys.* **2026**, *707*, A383. [CrossRef]
42. Gibbons, G.W.; Hawking, S.W. Cosmological event horizons, thermodynamics, and particle creation. *Phys. Rev. D* **1977**, *15*, 2738. [CrossRef]
43. Bekenstein, J.D. Black holes and entropy. *Phys. Rev. D* **1973**, *7*, 2333. [CrossRef]
44. Hawking, S.W. Particle creation by black holes. *Commun. Math. Phys.* **1975**, *43*, 199. [CrossRef]
45. Wald, R.M. Black hole entropy is the Noether charge. *Phys. Rev. D* **1993**, *48*, R3427. [CrossRef] [PubMed]
46. Padmanabhan, T. Thermodynamical aspects of gravity: New insights. *Rep. Prog. Phys.* **2010**, *73*, 046901. [CrossRef]
47. Padmanabhan, T. Equipartition of energy in the horizon degrees of freedom and the emergence of gravity. *Mod. Phys. Lett. A* **2010**, *25*, 1129. [CrossRef]
48. Verlinde, E.P. On the origin of gravity and the laws of Newton. *J. High Energy Phys.* **2011**, *2011*, 29. [CrossRef]
49. Padmanabhan, T. Emergence and expansion of cosmic space as due to the quest for holographic equipartition. *arXiv* **2012**. [CrossRef]
50. Casini, H.; Huerta, M. Entanglement entropy in free quantum field theory. *J. Phys. A Math. Theor.* **2009**, *42*, 504007. [CrossRef]
51. Donnelly, W.; Freidel, L. Local subsystems in gauge theory and gravity. *J. High Energy Phys.* **2016**, *2016*, 102. [CrossRef]
52. Harlow, D. Jerusalem lectures on black holes and quantum information. *Rev. Mod. Phys.* **2016**, *88*, 015002. [CrossRef]
53. Bombelli, L.; Koul, R.K.; Lee, J.; Sorkin, R.D. Quantum source of entropy for black holes. *Phys. Rev. D* **1986**, *34*, 373. [CrossRef] [PubMed]
54. Srednicki, M. Entropy and area. *Phys. Rev. Lett.* **1993**, *71*, 666. [CrossRef] [PubMed]

55. Susskind, L.; Uglum, J. Black hole entropy in canonical quantum gravity and superstring theory. *Phys. Rev. D* **1994**, *50*, 2700. [CrossRef] [PubMed]
56. Solodukhin, S.N. Entanglement entropy of black holes. *Living Rev. Relativ.* **2011**, *14*, 8. [CrossRef] [PubMed]
57. Cooperman, J.H.; Luty, M.A. Renormalization of entanglement entropy and the gravitational effective action. *J. High Energy Phys.* **2014**, *12*, 45. [CrossRef]
58. Engelhardt, N.; Wall, A.C. Quantum extremal surfaces: Holographic entanglement entropy beyond the classical regime. *J. High Energy Phys.* **2015**, *2015*, 73. [CrossRef]
59. Jacobson, T. Entanglement equilibrium and the Einstein equation. *Phys. Rev. Lett.* **2016**, *116*, 201101. [CrossRef] [PubMed]
60. Lashkari, N.; McDermott, M.B.; Van Raamsdonk, M. Gravitational dynamics from entanglement "thermodynamics". *J. High Energy Phys.* **2014**, *2014*, 195. [CrossRef]
61. Bousso, R. The holographic principle. *Rev. Mod. Phys.* **2002**, *74*, 825. [CrossRef]
62. Thorne, K.S.; Price, R.H.; Macdonald, D.A. *Black Holes: The Membrane Paradigm*; Yale University Press: New Haven, CT, USA, 1986.
63. Lee, J.-W.; Lee, J.; Kim, H.-C. Dark energy from vacuum entanglement. *J. Cosmol. Astropart. Phys.* **2007**, *2007*, 005. [CrossRef]
64. Lee, J.-W.; Kim, H.-C.; Lee, J. Gravity from quantum information. *J. Korean Phys. Soc.* **2013**, *63*, 1094. [CrossRef]
65. Bellini, E.; Sawicki, M. Maximal freedom at minimum cost: Linear large-scale structure in general modifications of gravity. *J. Cosmol. Astropart. Phys.* **2014**, *2014*, 050. [CrossRef]
66. Kase, R.; Tsujikawa, S. Dark energy in Horndeski theories after GW170817: A review. *Int. J. Mod. Phys. D* **2019**, *28*, 1942005. [CrossRef]
67. Wald, R.M. *General Relativity*; University of Chicago Press: Chicago, IL, USA, 1984.
68. Carroll, S.M. *Spacetime and Geometry: An Introduction to General Relativity*; Addison-Wesley: San Francisco, CA, USA, 2004.
69. Caldwell, R.R. A phantom menace? Cosmological consequences of a dark energy component with super-negative equation of state. *Phys. Lett. B* **2002**, *545*, 23. [CrossRef]
70. Vikman, A. Can dark energy evolve to the phantom? *Phys. Rev. D* **2005**, *71*, 023515. [CrossRef]
71. Gubitosi, G.; Piazza, F.; Vernizzi, F. The effective field theory of dark energy. *J. Cosmol. Astropart. Phys.* **2013**, *2013*, 032. [CrossRef]
72. Bloomfield, J.K.; Flanagan, E.E.; Park, M.; Watson, S. Dark energy or modified gravity? An effective field theory approach. *J. Cosmol. Astropart. Phys.* **2013**, *2013*, 010. [CrossRef]
73. Kobayashi, T.; Yamaguchi, M.; Yokoyama, J. Generalized G-inflation: Inflation with the most general second-order field equations. *Prog. Theor. Phys.* **2011**, *126*, 511. [CrossRef]
74. Deffayet, C.; Pujolàs, O.; Sawicki, I.; Vikman, A. Imperfect dark energy from kinetic gravity braiding. *J. Cosmol. Astropart. Phys.* **2010**, *2010*, 026. [CrossRef]
75. Peebles, P.J.E. *The Large-Scale Structure of the Universe*; Princeton University Press: Princeton, NJ, USA, 1980.
76. Dodelson, S. *Modern Cosmology*; Academic Press: Cambridge, MA, USA, 2003.
77. Linder, E.V. Cosmic growth history and expansion history. *Phys. Rev. D* **2005**, *72*, 043529. [CrossRef]
78. Kaiser, N. Clustering in real space and in redshift space. *Mon. Not. R. Astron. Soc.* **1987**, *227*, 1–21. [CrossRef]
79. Hamilton, A.J.S. Linear redshift distortions: A review. In *The Evolving Universe*; Hamilton, D., Ed.; Kluwer Academic Publishers: Dordrecht, The Netherlands, 1998; pp. 185–275. [CrossRef]
80. Casini, H.; Huerta, M.; Myers, R.C. Towards a derivation of holographic entanglement entropy. *J. High Energy Phys.* **2011**, *2011*, 36. [CrossRef]
81. Beach, M.J.S.; Lee, J.; Rabideau, C.; Van Raamsdonk, M. Entanglement entropy from one-point functions in holographic states. *J. High Energy Phys.* **2016**, *2016*, 85. [CrossRef]
82. Bhattacharya, J.; Nozaki, M.; Takayanagi, T.; Ugajin, T. Thermodynamical property of entanglement entropy for excited states. *Phys. Rev. Lett.* **2013**, *110*, 091602. [CrossRef] [PubMed]
83. Blanco, D.D.; Casini, H.; Hung, L.-Y.; Myers, R.C. Relative entropy and holography. *J. High Energy Phys.* **2013**, *2013*, 60. [CrossRef]
84. Herzog, C.P.; Huang, K.-W. Stress tensors from trace anomalies in conformal field theories. *Phys. Rev. D* **2013**, *87*, 081901. [CrossRef]
85. Jacobson, T. Black hole entanglement entropy and the renormalization group. *Phys. Rev. D* **2013**, *87*, 084047. [CrossRef]
86. Wall, A.C. A survey of black hole thermodynamics. *arXiv* **2018**. [CrossRef]
87. Brout, D.; Scolnic, D.; Popovic, B.; Riess, A.G.; Zuntz, J.; Kessler, R.; Carr, A.; Davis, T.M.; Hinton, S.; Jones, D.O.; et al. The Pantheon+ analysis: Cosmological constraints. *Astrophys. J.* **2022**, *938*, 110. [CrossRef]
88. Zhang, C.; Zhang, H.; Yuan, S.; Liu, S.; Zhang, T.-J.; Sun, Y.-C. Four new observational $H(z)$ data from luminous red galaxies in the Sloan Digital Sky Survey data release seven. *Res. Astron. Astrophys.* **2014**, *14*, 1221. [CrossRef]
89. Simon, J.; Verde, L.; Jimenez, R. Constraints on the redshift dependence of the dark energy potential. *Phys. Rev. D* **2005**, *71*, 123001. [CrossRef]

90. Moresco, M.; Cimatti, A.; Jimenez, R.; Pozzetti, L.; Zamorani, G.; Bolzonella, M.; Dunlop, J.; Lamareille, F.; Mignoli, M.; Pearce, H.; et al. Improved constraints on the expansion rate of the Universe up to $z \sim 1.1$ from the spectroscopic evolution of cosmic chronometers. *J. Cosmol. Astropart. Phys.* **2012**, *2012*, 006. [CrossRef]
91. Moresco, M.; Pozzetti, L.; Cimatti, A.; Jimenez, R.; Maraston, C.; Verde, L.; Thomas, D.; Citro, A.; Tojeiro, R.; Wilkinson, D. A 6% measurement of the Hubble parameter at $z \sim 0.45$: Direct evidence of the epoch of cosmic re-acceleration. *J. Cosmol. Astropart. Phys.* **2016**, *2016*, 014. [CrossRef]
92. Moresco, M. Raising the bar: New constraints on the Hubble parameter with cosmic chronometers at $z \sim 2$. *Mon. Not. R. Astron. Soc. Lett.* **2015**, *450*, L16. [CrossRef]
93. Ratsimbazafy, A.L.; Loubser, S.I.; Crawford, S.M.; Cress, C.M.; Bassett, B.A.; Nichol, R.C.; Väisänen, P. Age-dating luminous red galaxies observed with the Southern African Large Telescope. *Mon. Not. R. Astron. Soc.* **2017**, *467*, 3239. [CrossRef]
94. Stern, D.; Jimenez, R.; Verde, L.; Kamionkowski, M.; Stanford, S.A. Cosmic chronometers: Constraining the equation of state of dark energy. I: $H(z)$ measurements. *J. Cosmol. Astropart. Phys.* **2010**, *2010*, 008. [CrossRef]
95. Sanchez, A.G. et al. [BOSS Collaboration]. The clustering of galaxies in the SDSS-III Baryon Oscillation Spectroscopic Survey: Cosmological implications of the full shape of the clustering wedges in the data release 10 and 11 galaxy samples. *Mon. Not. R. Astron. Soc.* **2014**, *440*, 2692. [CrossRef]
96. Gil-Marín, H.; Percival, W.J.; Verde, L.; Brownstein, J.R.; Chuang, C.-H.; Kitaura, F.-S.; Rodríguez-Torres, S.A.; Olmstead, M.D. The clustering of galaxies in the SDSS-III Baryon Oscillation Spectroscopic Survey: RSD measurement from the power spectrum and bispectrum of the DR12 BOSS galaxies. *Mon. Not. R. Astron. Soc.* **2017**, *465*, 1757. [CrossRef]
97. Chuang, C.-H. et al. [BOSS Collaboration]. The clustering of galaxies in the SDSS-III Baryon Oscillation Spectroscopic Survey: Single-probe measurements from CMASS anisotropic galaxy clustering. *Mon. Not. R. Astron. Soc.* **2016**, *461*, 3781–3793. [CrossRef]
98. Beutler, F. et al. [BOSS Collaboration]. The clustering of galaxies in the completed SDSS-III Baryon Oscillation Spectroscopic Survey: Anisotropic galaxy clustering in Fourier-space. *Mon. Not. R. Astron. Soc.* **2017**, *466*, 2242–2260. [CrossRef]
99. Wang, Y.; Zhao, G.-B.; Chuang, C.-H.; Pellejero-Ibanez, M.; Zhao, C.; Kitaura, F.-S.; Rodriguez-Torres, S. The clustering of galaxies in the completed SDSS-III Baryon Oscillation Spectroscopic Survey: A tomographic analysis of structure growth and expansion rate from anisotropic galaxy clustering. *Mon. Not. R. Astron. Soc.* **2018**, *481*, 3160–3166. [CrossRef]
100. Tojeiro, R. et al. [BOSS Collaboration]. The clustering of galaxies in the SDSS-III Baryon Oscillation Spectroscopic Survey: Measuring structure growth using passive galaxies. *Mon. Not. R. Astron. Soc.* **2012**, *424*, 2339–2344. [CrossRef]
101. Blake, C.; Brough, S.; Colless, M.; Contreras, C.; Couch, W.; Croom, S.; Croton, D.; Davis, T.M.; Drinkwater, M.J.; Forster, K.; et al. The WiggleZ Dark Energy Survey: Joint measurements of the expansion and growth history at $z < 1$. *Mon. Not. R. Astron. Soc.* **2012**, *425*, 405–414. [CrossRef]
102. de la Torre, S.; Guzzo, L.; Peacock, J.A.; Branchini, E.; Iovino, A.; Granett, B.R.; Abbas, U.; Adami, C.; Arnouts, S.; Bel, J.; et al. The VIMOS Public Extragalactic Redshift Survey (VIPERS). Galaxy clustering and redshift-space distortions at $z = 0.8$ in the first data release. *Astron. Astrophys.* **2013**, *557*, A54. [CrossRef]
103. Wilson, M.J. Geometric and Growth Rate Tests of General Relativity with Recovered Linear Cosmological Perturbations. Ph.D. Thesis, University of Edinburgh, Edinburgh, UK, 2017. [CrossRef]
104. Hawken, A.J.; Granett, B.R.; Iovino, A.; Guzzo, L.; Peacock, J.A.; de la Torre, S.; Garilli, B.; Bolzonella, M.; Scodeggio, M.; Abbas, U.; et al. The VIMOS Public Extragalactic Redshift Survey: Measuring the growth rate of structure around cosmic voids. *Astron. Astrophys.* **2017**, *607*, A54. [CrossRef]
105. de la Torre, S.; Jullo, E.; Giocoli, C.; Pezzotta, A.; Bel, J.; Granett, B.R.; Guzzo, L.; Garilli, B.; Scodeggio, M.; Bolzonella, M.; et al. The VIMOS Public Extragalactic Redshift Survey (VIPERS). Gravity test from the combination of redshift-space distortions and galaxy–galaxy lensing at $0.5 < z < 1.2$. *Astron. Astrophys.* **2017**, *608*, A44. [CrossRef]
106. Pezzotta, A.; de la Torre, S.; Bel, J.; Granett, B.R.; Guzzo, L.; Peacock, J.A.; Garilli, B.; Scodeggio, M.; Bolzonella, M.; Abbas, U.; et al. The VIMOS Public Extragalactic Redshift Survey (VIPERS): The growth of structure at $0.5 < z < 1.2$ from redshift-space distortions in the clustering of the PDR-2 final sample. *Astron. Astrophys.* **2017**, *604*, A33. [CrossRef]
107. Mohammad, F.G.; Granett, B.R.; Guzzo, L.; Bel, J.; Branchini, E.; De La Torre, S.; Moscardini, L.; Peacock, J.A.; Bolzonella, M.; Garilli, B.; et al. The VIMOS Public Extragalactic Redshift Survey (VIPERS). An unbiased estimate of the growth rate of structure at $\langle z \rangle = 0.85$ using the clustering of luminous blue galaxies. *Astron. Astrophys.* **2018**, *610*, A59. [CrossRef]
108. Howlett, C.; Staveley-Smith, L.; Elahi, P.J.; Hong, T.; Jarrett, T.H.; Jones, D.H.; Koribalski, B.S.; Macri, L.M.; Masters, K.L.; Springob, C.M. 2MTF–VI. Measuring the velocity power spectrum. *Mon. Not. R. Astron. Soc.* **2017**, *471*, 3135–3151. [CrossRef]
109. Davis, M.; Nusser, A.; Masters, K.; Springob, C.; Huchra, J.P.; Lemson, G. Local gravity versus local velocity: Solutions for β and nonlinear bias. *Mon. Not. R. Astron. Soc.* **2011**, *413*, 2906–2922. [CrossRef]
110. Hudson, M.J.; Turnbull, S.J. The growth rate of cosmic structure from peculiar velocities at low and high redshifts. *Astrophys. J. Lett.* **2013**, *751*, L30. [CrossRef]
111. Beutler, F.; Blake, C.; Colless, M.; Jones, D.H.; Staveley-Smith, L.; Poole, G.B.; Campbell, L.; Parker, Q.; Saunders, W.; Watson, F. The 6dF Galaxy Survey: $z \approx 0$ measurement of the growth rate and σ_8. *Mon. Not. R. Astron. Soc.* **2012**, *423*, 3430–3444. [CrossRef]

112. Huterer, D.; Shafer, D.; Scolnic, D.; Schmidt, F. Testing ΛCDM at the lowest redshifts with SN Ia and galaxy velocities. *J. Cosmol. Astropart. Phys.* **2017**, *2017*, 015. [CrossRef]
113. Okumura, T.; Hikage, C.; Totani, T.; Tonegawa, M.; Okada, H.; Glazebrook, K.; Blake, C.; Ferreira, P.G.; More, S.; Taruya, A.; et al. The Subaru FMOS galaxy redshift survey (FastSound). IV. New constraint on gravity theory from redshift space distortions at $z\sim$1.4. *Publ. Astron. Soc. Jpn.* **2016**, *68*, 38. [CrossRef]
114. Zhao, G.-B. et al. [eBOSS Collaboration]. The clustering of the SDSS-IV Extended Baryon Oscillation Spectroscopic Survey DR14 quasar sample: A tomographic measurement of cosmic structure growth and expansion rate based on optimal redshift weights. *Mon. Not. R. Astron. Soc.* **2019**, *482*, 3497. [CrossRef]
115. Gil-Marín, H. et al. [eBOSS Collaboration]. The clustering of the SDSS-IV Extended Baryon Oscillation Spectroscopic Survey DR14 quasar sample: Structure growth rate measurement from the anisotropic quasar power spectrum in the redshift range $0.8 < z < 2.2$. *Mon. Not. R. Astron. Soc.* **2018**, *477*, 1604. [CrossRef]
116. Hou, J. et al. [eBOSS Collaboration]. The clustering of the SDSS-IV Extended Baryon Oscillation Spectroscopic Survey DR14 quasar sample: Anisotropic clustering analysis in configuration space. *Mon. Not. R. Astron. Soc.* **2018**, *480*, 2521. [CrossRef]
117. Kazantzidis, L.; Perivolaropoulos, L. Evolution of the $f\sigma_8$ tension with the Planck15/ΛCDM determination and implications for modified gravity theories. *Phys. Rev. D* **2018**, *97*, 103503. [CrossRef]
118. Song, Y.-S.; Percival, W.J. Reconstructing the history of structure formation using redshift distortions. *J. Cosmol. Astropart. Phys.* **2009**, *2009*, 004. [CrossRef]
119. Samushia, L.; Percival, W.J.; Raccanelli, A. Interpreting large-scale redshift-space distortion measurements. *Mon. Not. R. Astron. Soc.* **2012**, *420*, 2102–2119. [CrossRef]
120. Chuang, C.-H.; Wang, Y. Modeling the anisotropic two-point galaxy correlation function on small scales and improved measurements of $H(z)$, $D_A(z)$, and $\beta(z)$ from the Sloan Digital Sky Survey DR7 luminous red galaxies. *Mon. Not. R. Astron. Soc.* **2013**, *435*, 255. [CrossRef]
121. Howlett, C.; Ross, A.; Samushia, L.; Percival, W.; Manera, M. The clustering of the SDSS main galaxy sample–II. Mock galaxy catalogues and a measurement of the growth of structure from redshift space distortions at $z = 0.15$. *Mon. Not. R. Astron. Soc.* **2015**, *449*, 848. [CrossRef]
122. Feix, M.; Nusser, A.; Branchini, E. Growth rate of cosmological perturbations at $z\sim$0.1 from a new observational test. *Phys. Rev. Lett.* **2015**, *115*, 011301. [CrossRef] [PubMed]
123. Feix, M.; Branchini, E.; Nusser, A. Speed from light: Growth rate and bulk flow at $z\sim$0.1 from improved SDSS DR13 photometry. *Mon. Not. R. Astron. Soc.* **2017**, *468*, 1420–1425. [CrossRef]
124. Blake, C.; Baldry, I.K.; Bland-Hawthorn, J.; Christodoulou, L.; Colless, M.; Conselice, C.; Driver, S.P.; Hopkins, A.M.; Liske, J.; Loveday, J.; et al. Galaxy and Mass Assembly (GAMA): Improved cosmic growth measurements using multiple tracers of large-scale structure. *Mon. Not. R. Astron. Soc.* **2013**, *436*, 3089–3105. [CrossRef]
125. Shi, F.; Yang, X.; Wang, H.; Zhang, Y.; Mo, H.J.; Bosch, F.C.v.D.; Luo, W.; Tweed, D.; Li, S.; Liu, C.; et al. Mapping the real space distributions of galaxies in SDSS DR7: II. Measuring the growth rate, clustering amplitude of matter and biases of galaxies at redshift 0.1. *Astrophys. J.* **2018**, *861*, 137. [CrossRef]
126. Foreman-Mackey, D.; Hogg, D.W.; Lang, D.; Goodman, J. `emcee`: The MCMC Hammer. *Publ. Astron. Soc. Pac.* **2013**, *125*, 306–312. [CrossRef]
127. Lewis, A. GetDist: A Python package for analysing Monte Carlo samples. *J. Cosmol. Astropart. Phys.* **2025**, *2025*, 025. [CrossRef]
128. Akaike, H. A new look at the statistical model identification. *IEEE Trans. Autom. Control* **1974**, *19*, 716–723. [CrossRef]
129. Schwarz, G. Estimating the dimension of a model. *Ann. Stat.* **1978**, *6*, 461–464. [CrossRef]
130. Liddle, A.R. How many cosmological parameters? *Mon. Not. R. Astron. Soc.* **2004**, *351*, L49–L53. [CrossRef]
131. Liddle, A.R. Information criteria for astrophysical model selection. *Mon. Not. R. Astron. Soc. Lett.* **2007**, *377*, L74–L78. [CrossRef]
132. Moresco, M.; Jimenez, R.; Verde, L.; Cimatti, A.; Pozzetti, L. Setting the Stage for Cosmic Chronometers. II. Impact of Stellar Population Synthesis Models Systematics and Full Covariance Matrix. *Astrophys. J.* **2020**, *898*, 82. [CrossRef]
133. Forero-Sánchez, D.; Rashkovetskyi, M.; Alves, O.; de Mattia, A.; Nadathur, S.; Zarrouk, P.; Gil-Marín, H.; Ding, Z.; Yu, J.; Andrade, U.; et al. Analytical and EZmock covariance validation for the DESI 2024 results. *J. Cosmol. Astropart. Phys.* **2025**, *2025*, 055. 10.1088/1475-7516/2025/04/055. [CrossRef]
134. Asgari, M.; Lin, C.-A.; Joachimi, B.; Giblin, B.; Heymans, C.; Hildebrandt, H.; Kannawadi, A.; Stölzner, B.; Tröster, T.; Busch, J.L.v.D.; et al. KiDS-1000 cosmology: Cosmic shear constraints and comparison between two-point statistics. *Astron. Astrophys.* **2021**, *645*, A104. [CrossRef]
135. Heymans, C.; Tröster, T.; Asgari, M.; Blake, C.; Hildebrandt, H.; Joachimi, B.; Kuijken K.; Lin, C.-A.; Sánchez, A.G.; Busch, J.L.v.D.; et al. KiDS-1000 cosmology: Multi-probe weak gravitational lensing and spectroscopic galaxy clustering constraints. *Astron. Astrophys.* **2021**, *646*, A140. [CrossRef]

136. Secco, L.F.; Samuroff, S.; Krause, E.; Jain, B.; Blazek, J.; Raveri, M.; Campos, A.; Amon, A.; Chen, A.; Doux, C.; et al. Dark Energy Survey Year 3 results: Cosmology from cosmic shear and robustness to modeling uncertainty. *Phys. Rev. D* **2022**, *105*, 023515. [CrossRef]
137. Madhavacheril, M.S. et al. [ACT Collaboration]. The Atacama Cosmology Telescope: DR6 gravitational lensing map and cosmological parameters. *Astrophys. J.* **2024**, *962*, 113. [CrossRef]
138. Carron, J.; Mirmelstein, M.; Lewis, A. CMB lensing from Planck PR4 maps. *J. Cosmol. Astropart. Phys.* **2022**, *2022*, 039. [CrossRef]
139. Hikage, C. et al. [HSC Collaboration]. Cosmology from cosmic shear power spectra with Subaru Hyper Suprime-Cam first-year data. *Publ. Astron. Soc. Jpn.* **2019**, *71*, 43. [CrossRef]
140. Crittenden, R.G.; Turok, N. Looking for a cosmological constant with the Rees–Sciama effect. *Phys. Rev. Lett.* **1996**, *76*, 575. [CrossRef] [PubMed]
141. Afshordi, N.; Loh, Y.-S.; Strauss, M.A. Cross-correlation of the Cosmic Microwave Background with the 2MASS galaxy survey: Signatures of dark energy, hot gas, and point sources. *Phys. Rev. D* **2004**, *69*, 083524. [CrossRef]
142. Giannantonio, T.; Scranton, R.; Crittenden, R.G.; Nichol, R.C.; Boughn, S.P.; Myers, A.D.; Richards, G.T. Combined analysis of the integrated Sachs–Wolfe effect and cosmological implications. *Phys. Rev. D* **2008**, *77*, 123520. [CrossRef]
143. Krolewski, A.; Ferraro, S. The integrated Sachs–Wolfe effect: unWISE and Planck constraints on dynamical dark energy. *J. Cosmol. Astropart. Phys.* **2022**, *2022*, 033. [CrossRef]
144. Ade, P.A.R. et al. [Planck Collaboration]. Planck 2015 results. XXI. The integrated Sachs–Wolfe effect. *Astron. Astrophys.* **2016**, *594*, A21. [CrossRef]
145. Das, S.; Souradeep, T. Suppressing CMB low multipoles with ISW effect. *J. Cosmol. Astropart. Phys.* **2014**, *2014*, 002. [CrossRef]
146. SDSS-IV Collaboration. Final BAO and RSD Measurements. Available online: https://www.sdss4.org/science/final-bao-and-rsd-measurements/ (accessed on 23 October 2025).
147. Turnbull, S.J.; Hudson, M.J.; Feldman, H.A.; Hicken, M.; Kirshner, R.P.; Watkins, R. Cosmic flows in the nearby Universe from Type Ia Supernovae. *Mon. Not. R. Astron. Soc.* **2012**, *420*, 447. [CrossRef]

Disclaimer/Publisher's Note: The statements, opinions and data contained in all publications are solely those of the individual author(s) and contributor(s) and not of MDPI and/or the editor(s). MDPI and/or the editor(s) disclaim responsibility for any injury to people or property resulting from any ideas, methods, instructions or products referred to in the content.